Summer 8-7-2020

# Electrostatic Denaturation of DNA-Cisplatin Adducts

Eddie Madrigal
*University of San Francisco*, eddie.madrigal333@gmail.com

## Recommended Citation

Madrigal, Eddie, "Electrostatic Denaturation of DNA-Cisplatin Adducts" (2020). *Master's Theses*. 1326.
https://repository.usfca.edu/thes/1326

# Electrostatic Denaturation of DNA-Cisplatin Adducts

A thesis presented to the faculty of the Department of Chemistry at the University of San Francisco in partial fulfillment of the requirements for the degree of

**Master of Science in Chemistry**

Written by

Eddie Madrigal
Bachelor of Science in Chemistry
Saint Mary’s College of California- Moraga, CA

August 7th, 2020

# Electrostatic Denaturation of DNA/Cisplatin Adducts

Thesis written by Eddie Madrigal

This thesis is written under the guidance of the Faculty Advisory Committee, and approved by all its members, has been accepted in partial fulfillment of the requirements for the degree of

**Master of Science in Chemistry at the University of San Francisco**

Thesis Committee

Ryan M. West, Ph.D. Date
Research Advisor

Osasere Evbuomwan, Ph.D. Date
Assistant Professor

Lawrence Margerum, Ph.D. Date
Professor

Marcelo Camperi, Ph.D. Date
Dean, College of Arts and Sciences

# Acknowledgement

First, I want to thank Dr. West for his mentorship, guidance and trust during my time at the University of San Francisco. I am honored to be apart of the West Lab and work with you during my time at the University San Francisco. I also want to thank Dr. Evbuomwan and Dr. Margerum for being a part of my thesis committee. Thank you to all the chemistry faculty and staff including Deidre Shymanski, Jeff Oda, Angela Qin and Matt Helm for helping me with equipment, chemicals, and planning I needed to do my research at the University of San Francisco. A special thanks to all my fellow students in the West lab including Wesley, Jeffrey, Gayatri, Farhad, Nutthakarn, Ziming, Amanda, Lucas, and Phaedra for your help and company during research.

# Table of Contents

# Table of Figures

## List of Equations

## List of Tables

# Abstract

In this thesis, electrochemical approaches are used to determine the properties of deoxyribonucleic acid (DNA) by electrostatic denaturation. The electrochemical routine involves an application of a destabilization potential, an equilibration potential, and a square wave voltammogram (SWV) to monitor the extent of melting. Our method uses a monolayer consisting of thiol modified DNA and mercaptohexanol on a gold electrode. These electrodes are then incubated in a complementary sequence tagged with methylene blue. By using our electrostatic denaturation technique, different parameters are explored, such as surface densities, surface coverages, and ionic strengths. As proof of concept, these techniques were applied toward detecting cisplatin interactions on a DNA surface. Depending on the surface coverage, cisplatin changes DNA stability accordingly.

# Chapter 1 Electrochemical Biosensors

## *1.1 Chemical Sensors*

Chemical sensors are a powerful tool used to convert a chemical or physical change into a measurable signal [1]. These sensors are designed to detect a specific analyte and minimize interference from other compounds. A biosensor is a chemical sensor that utilizes a biologically derived analyte from a biological system and/or detects such molecules. Once the sensor detects an analyte, a part of the sensor called a transducer produces a signal. The signal is then transferred to a signal processor, which amplifies and displays the resulting signal.

An electrochemical biosensor is a subclass of a biosensor that uses an electrochemical method for signal transduction, typically measuring changes in current or potentials to detect the presence of a specific biological molecule. A schematic of an electrochemical biosensor can be seen in Figure 1. An electrochemical biosensor can be further broken down into two different types. These types are biocatalytic devices and affinity sensors. A biocatalytic device utilizes an enzyme or cell to recognize and react with the specific analyte and produces an electroactive species as a product [1]. This product is typically the measured species. The most common and commercially successful example of this type of electrochemical biosensor is a glucose meter. Other examples include lactose and xanthine meters [1]. On the other hand, an affinity biosensor relies on the analyte binding to a biological component, such as an antibody or DNA strand, to produce a signal. The work presented in this thesis is based on DNA hybridization affinity sensing.

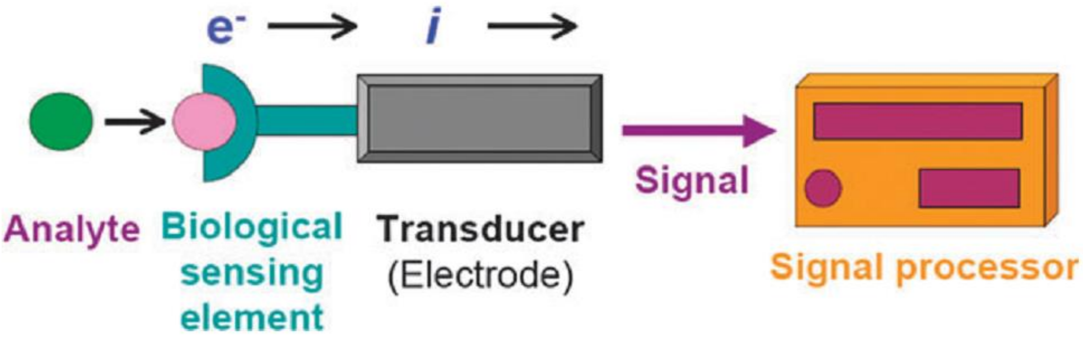

**Figure 1:** A schematic of an electrochemical biosensor [1].

### *1.2 A Brief Description of Biocatalytic Devices and Affinity Censors.*

The history of glucose meters dates to 1962 when the first sensors were developed at the Cincinnati Children's Hospital [2]. The first generation of glucose meters consisted of a layer of the enzyme glucose oxidase, $GO_x$, on an oxygen-sensitive electrode by use of a semipermeable membrane [1,2]. When glucose is introduced, oxygen is consumed by $GO_x$, leading to a detectable change in oxygen concentration at the electrode. The reaction is shown in Equation 1. The consumption of glucose also leads to the formation of hydrogen peroxide, $H_2O_2$. Hydrogen peroxide is electrochemically active and, more recently, has been used to detect the presence of glucose. The oxidation of $H_2O_2$ can be seen in equation 2:

$$\text{glucose} + O_2 \xrightarrow{\text{glusoce oxidase}} \text{gluconic acid} + H_2O_2 \tag{1}$$

$$H_2O_2 \rightarrow O_2 + 2H^+ + 2e^- \tag{2}$$

Another type of biosensor is the affinity sensor. An affinity sensor uses the specificity of biomolecular interactions, such as the interactions between an antibody and antigen, to improve selectivity. Thus, the electrode is typically modified with a macro biomolecule to serve as a recognition element. The electrochemical measurement must be designed such that the binding of this analyte causes an electrical signal to be created. The recognition of this analyte is often determined by the shape of the analyte or the shape of the analyte and recognition element. These specifications make the affinity sensor highly selective and sensitive [1].

A common type of affinity sensor is an immunosensor. An immunosensor uses antibodies to detect an antigen sample. For instance, Ligar et al. examined a fluorescence-based immunosensor that is used to detect antigens [3]. *Yersinia. pestis* (*Y. pestis*) is one of the main bacteria that caused the Black Death to occur in the 14th century. The F1 antigen is a major component of *Y. pestis* and is secreted in the species once *Y. pestis* has invaded a mammalian host. In this experiment, the F1 antigen was being detected, and monoclonal antibodies were used as a recognition element. F1 antigen was spiked into six different biological samples, saliva, nasal, urine, serum, plasma, and blood. A buffer sample was also prepared to act as a control. Four different concentrations of antigen were used 0, 25,125, and 625 ng/mL. The samples were then assayed on slides to detect F1 antigen. The results can be seen in Figure 2 [3]. When comparing the two high concentrations of 125 and 625 ng/mL, a 5-fold increase in concentration only led to a 2.3-fold increase in normalized signal. Ligar et al. determined that the use of a fluorescence-based immunosensor can detect F1 antigen as low as 25 ng/mL in all matrix solutions.

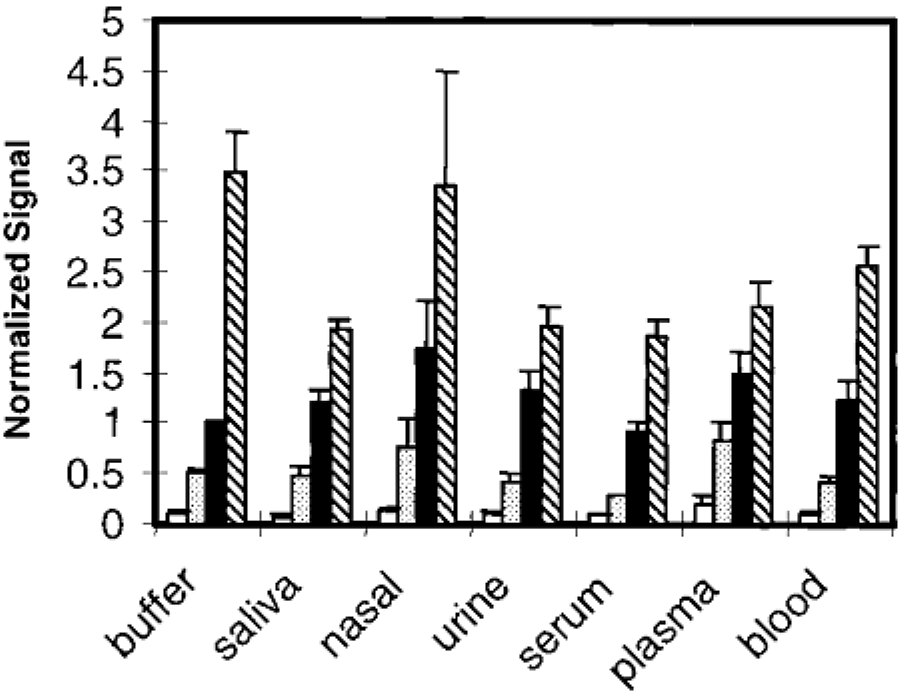

**Figure 2:** F1 antigen was spiked into 7 different solutions each at different concentration: 0 (blank), 25 (dotted), 125 (black), and 625 (stripe) ng/mL. Each bar is the mean normalized plot for 4 samples. Detection of F1 antigen can be seen as low as 25 ng/mL [3].

Another type of affinity sensor is a DNA biosensor. The type of DNA biosensor most relevant in this work is a DNA hybridization biosensor. In a hybridization biosensor, a short DNA sequence, usually around 20 to 40 base pairs, is immobilized on the electrode surface. A signal is produced when the complementary strand attaches to the bounded strand [4]. This binding of the two strands is called hybridization. The complementary strand often has an electrochemically-active label (also known as a “tag”) on it that allows the creation of an electrochemical signal. There are many ways to create a DNA biosensor, but some commonalities are that they contain an immobilized sequence called probe, a complementary sequence called target, a passivation layer to prevent non-specific adsorption of the DNA. Furthermore, many involve a redox-active label that is either covalently attached or specifically binds to double-stranded DNA [4]. DNA biosensors have many applications, including in the food and environmental industries. They allow one to obtain sequence-specific information rapidly and at a lower potential cost than other traditional benchtop methods. Also, unlike the enzyme-based sensors such as a glucose meter, or the antibody meters, DNA sensors can be regenerated and used multiple times and are typically more stable [4]. This research uses electrochemical techniques to do an in-depth analysis of detected DNA via electric field-induced melting.

## Chapter 2: Electrochemical Concepts

To better understand the structure and stability of DNA, electrochemical techniques can be used. The understanding of the physical and chemical properties of DNA at an electrochemical interface is necessary to optimize DNA biosensors. Thus, it is essential to understand electrochemical techniques to get a better understanding of how electrochemical DNA biosensors work. This section will cover the following: (1) electrochemical concepts such as electrochemical cell and electrochemical equilibrium, (2) electrochemical techniques, their usage and purpose.

### *2.1 Electrochemical Equilibrium*

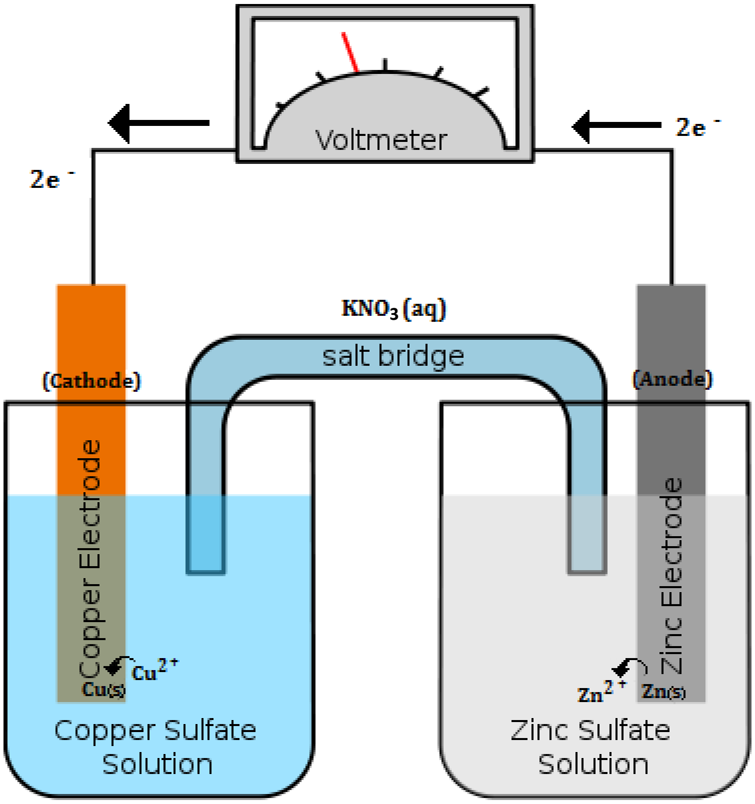

**Figure 3:** Schematic of a galvanic cell. When the copper cathode and zinc anode are connected, electrons flow and potential is measured by a voltmeter. [5]

Electrochemistry involves the measurement of electrical potentials or currents related to chemical processes that occur at the interface of electrical conductors and electrolyte solutions. These currents and potentials are measured through the transfer of electrons. This transfer of electrons can be separated into two separate reactions. When a substance gains an electron, the element is reduced. When a substance loses an electron, the element is oxidized [5]. In electrochemistry, the transfer of electrons occurs at an electrode. The electrode at which a substance (analyte of interest) gets reduced is called the cathode, while the electrode at which a substance gets oxidized is called the anode. This flow of electrons occurs by cations flowing to the cathode and cations leaving the anode. To balance each side, counterions are added as well. Each one of these vessels containing an electrode and an electrolyte solvent is called a half cell. Two half cells can be seen in Figure 3. In Figure 3, the Zn(s) is oxidized producing $Zn^{2+}$. Likewise, the $Cu^{2+}$ is reduced and Cu(s) is deposited on solid copper. These two relationships can be seen in equations 3 and 4:

$$\mathrm{Zn(s)} \rightarrow \mathrm{Zn^{2+}(aq)} + 2e^- \tag{3}$$

$$\mathrm{Cu^{2+}(aq)} + 2e^- \rightarrow \mathrm{Cu(s)} \tag{4}$$

The oxidation of zinc creates a positive charge at the electrode surface while a negative charge is created in the copper solution. Since a neutral charge is needed for the proper function of a galvanic cell, a salt bridge is added. For oxidation and reduction to take place, the two cells must be connected by a close circuit which allows electrons to flow. This electron transfer from the anode to the cathode causes electrical energy stored on each electrode to be utilized to pushed electrons through an external circuit. The difference in electrical potential between these two interfaces is known as the cell potential. A shorthand notation, called cell notation or a cell diagram, is shown below in equation 5, where Zn(s) represents the anode, the $Zn^{2+}$ represents the solution of the anode, the $Cu^{2+}$ represents the solution of the cathode and the Cu(s) represents the cathode.

$$\mathrm{Zn(s)|Zn^{2+}||Cu^{2+}|Cu(s)} \tag{5}$$

The single dash line represents a phase change and the double dash lines represent a salt bridge connection. The cell described in equation 3 is known as a galvanic cell. If an outside electrical source is used to drive the redox reaction, the cell is called an electrolytic cell [6]. An example of an electrolytic cell would be a rechargeable battery. Once a battery runs out of power, all the electrons have transferred from the anode to the cathode. To recharge the battery, an electrolytic cell is created, and an outside power source transfers the electrons from the cathode to the anode [6].

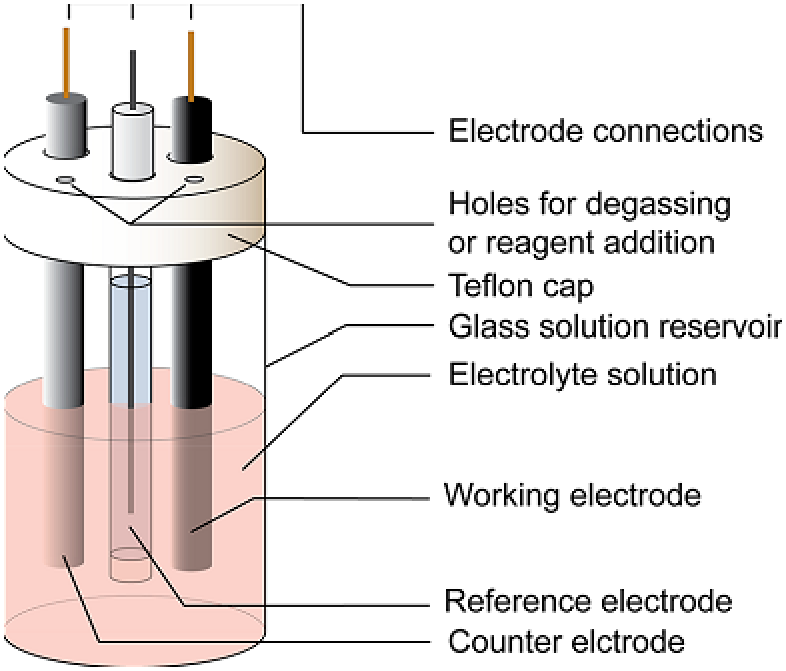

**Figure 4**: A schematic of a three-electrode system. A reference, working and counter electrode are connected to a potentiostat to apply a voltage between the working and references electrodes. [7]

A more common system used today for electrochemical measurements is a three-electrode cell. A three-electrode system, as seen in Figure 4, consists of the working, counter and reference electrode. The reaction of interest takes place at the working electrode and potentials are applied to this electrode relative to the reference electrode. A reference electrode is a half-cell where a stable reversable redox reaction takes place separated from the sample by a salt bridge. Potentials on the working electrode are measured or applied in reference to this electrode.

One of the first reference electrodes was the standard hydrogen electrode, or S.H.E. This redox reaction is defined as the following:

$$2\mathrm{H}^+(\mathrm{aq}) + 2\mathrm{e}^- \rightleftharpoons \mathrm{H}_2(\mathrm{g}) \tag{6}$$

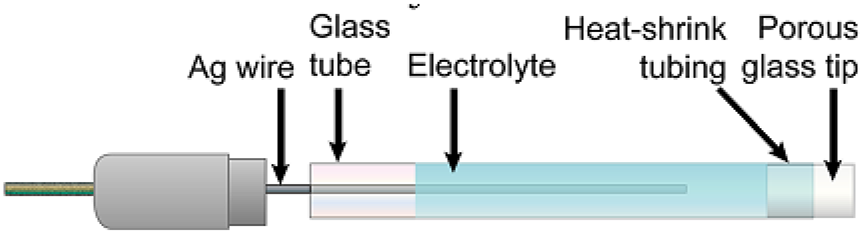

**Figure 5**: A redox reaction occurs between the silver and the silver chloride at the electrode, resulting in formation of standard reduction potential. [7]

The S.H.E is assigned a potential of zero volts. This means that if a potential measured at a working electrode reads a voltage of + 0.3 V while using S.H.E, then the potential is positive 0.3 V of the S.H.E. The actual potential at the electrode, and even the charge of the electrode is not readily determined; much like energies, potentials are only known in reference to a reference potential. One disadvantage of using the S.H.E is that it is difficult to set up in a three-electrode system [7]. Another type of reference electrode is the silver-silver chloride reference electrode, as seen in Figure 5. The silver-silver chloride reference electrode consists of silver wire coated with silver chloride immersed in a solution of potassium and silver chloride. The half reaction can be seen in Equation 7:

$$\mathrm{AgCl}(s) + e^{-} - \rightleftharpoons \mathrm{Ag}(s) + Cl^{-}(aq) \quad (7)$$

With saturated potassium chloride, ~ 3 M, the standard reduction potential of the reference electrode is +0.197 V in relationship to the S.H.E. [7]. A counter or auxiliary electrode, is used to complete the circuit between the working electrode, electrolyte, and the potentiostat. It closes the loop of the electrical current. It is important for the counter electrode to be an inert metal to prevent generation of byproducts that could interfere with the reactions of the working electrode. A common counter electrode used in a three-electrode system is platinum.

Under standard conditions, the cell potential can be represented by Equation 8, where $E^o$ (reduction) and $E^o$ (oxidation) represent the reduction and oxidation electrical energy respectively.

$$\mathrm{E^o} = \mathrm{E^o}\ (\mathrm{reduction}) - \mathrm{E^o}\ (\mathrm{oxidation}) \quad (8)$$

Thermodynamically, $E^o$ is related to $\Delta G^o$ by Equation 9. Where $\Delta G^o$ is Gibbs free energy at standard conditions, n is the number of electrons transferred in a balanced equation, F is Faraday's constant (96485 C $mol^{-1}$) and $E^o$ is the potential difference at standard conditions. If $E^o$ is positive, the reaction is spontaneous while if $E^o$ is negative, the reaction is nonspontaneous. Under non-standard conditions, the relationship between E and Delta G is given in equation 10:

$$\Delta \mathrm{G^o} = -\mathrm{nFE^o} \quad (9)$$

$$\Delta \mathrm{G} = -\mathrm{nFE} \quad (10)$$

By substituting Equation 9 and 10 into the Gibbs free energy change under nonstandard conditions Equation 11 is derived. Where R is a constant of 8.314 J/mol K, and Q is the reaction quotient.

$$\mathrm{E} = E^{o} - (\mathrm{RT/nF})\ \mathrm{lnQ} \tag{11}$$

As the reaction reaches equilibrium, Q = K and ΔG = 0 thus E = 0. Knowing this, Equation 11 can be rewritten as Equation 12 here where K is the equilibrium constant.

$$\log(\mathrm{K}) = \mathrm{nE^{o}}/0.0592\mathrm{V} \tag{12}$$

Equation 12 indicates that K is proportional to $E^o$. If $E^o$ is positive, K is greater than 1 and the reaction favors the products. If $E^o$ is negative, K is less than 1 and the reaction favors the reactants [8].

Anytime an electrode is inserted in an electrolyte solution, an interfacial potential will develop as charge separates across the interface. To counter that charge, a set potential can be applied to the electrode until the total voltage is zero [9]. This point is called the point of zero charge. If a more negative potential is applied then the point of zero charge, the electrode will have a negatively charged surface. A more positive potential will cause the surface to have a positively charged surface. Note, these charges are absolute, unlike the potentials, which are relative. Also note that the point of zero charge is different than the cell potential in most systems.

### *2.2 Surface Reactions (Electrochemical Double Layer)*

When a metal electrode is placed in an electrolyte solution, the various charges and dipoles in the solution will reorient and redistribute. As this process occurs, electrons located in a negatively charged electrode (point more negative than the point of zero charge) will create a layer that is equal to the charge of cations in solution. This formation of an ionic layer that is equal and opposite of the ions in the metal is called a double-layer. The double-layer can further be divided into three different layers, the Inner Helmholtz Plane (IHP), Outer Helmholtz Plane (OHP), and the diffusion layer. The IHP consists of ions of opposite charge of the metal (and possible neutral species, as well) and is distance $d_1$ from the electrode surface. The OHP consist of the ions surrounded by solvent molecules. These solvated molecules can only approach the surface of the electrode distance $d_2$. Finally, the diffusion layer consists of solvated ions attracted to the electrode surface through weak electrostatic forces. Due to the fact that attraction forces on the diffusion layer are weaker, these ions move freely in solution. The thickness and structure of the double-layer depends on the ionic strength of the solvent used. A schematic of the electrode double layer can be seen in Figure 6.

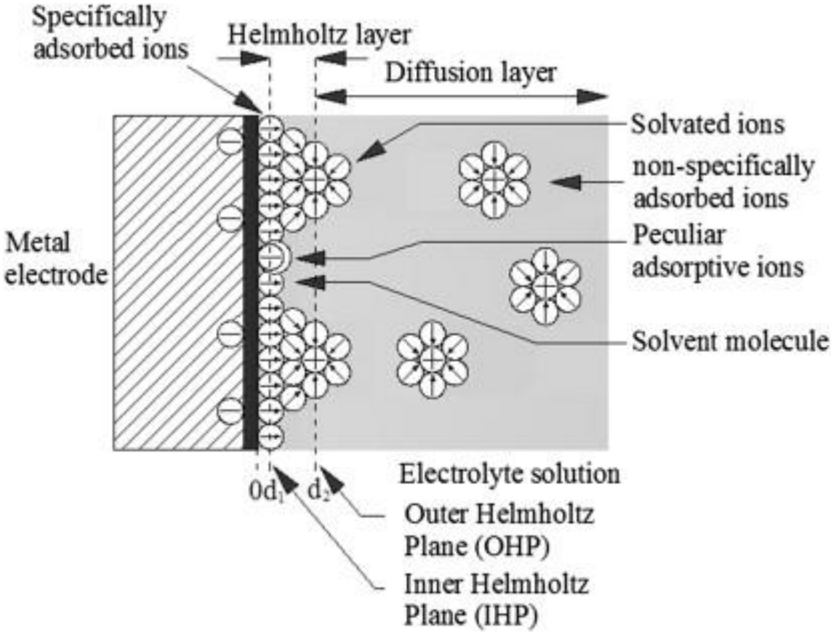

**Figure 6**: A schematic showing the approximate distances of the IHP, OHP and diffusion layer. As ions and solvent molecules move away from the electrode surface, electric fields are less pronounced [11].

### *2.3 Electrochemical Technique*

When running electrochemical experiments, an instrument called a potentiostat must be used. A potentiostat controls or measures the voltage between a working and counter electrode pair. It forces or measures a current through the working electrode [10]. This current and potential are then recorded and analyzed. Depending on the goal of the experiment, different electrochemical techniques can be used. Some common techniques are chronoamperometry, cyclic voltammetry, and square wave voltammetry.

Chronoamperometry (CA) is an electrochemical technique in which the potential is stepped from an initial potential to another potential and current is measured versus time. CA is useful for quantitatively analyzing redox reactions. An initial potential, where no redox reaction

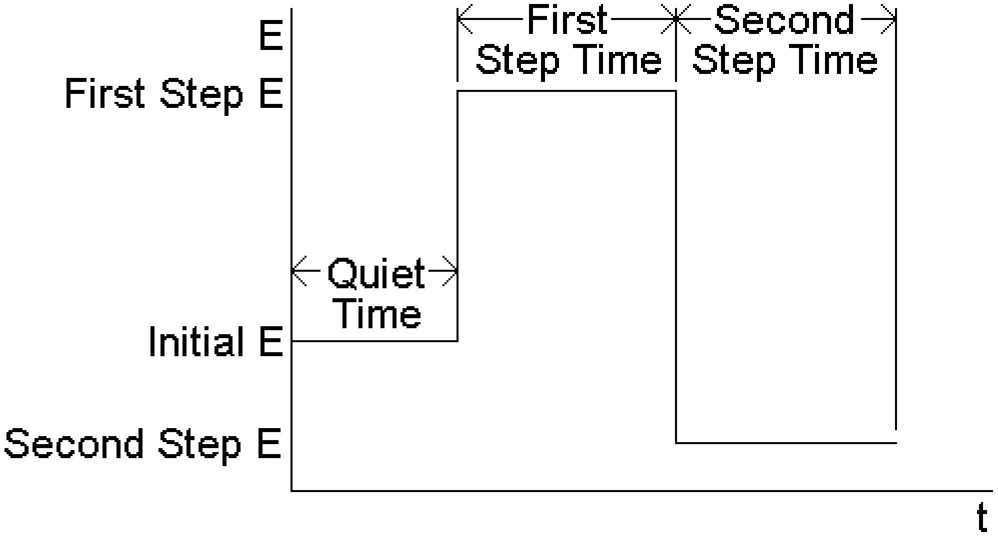

**Figure 7**: Schematic of chronoamperometry. Quiet time represents the time at the initial potential and each step represents a different potential [12].

occurs, is applied and then stepped up or down to a potential where reduction or oxidation is very fast (current limited by diffusion to the electrode surface) and the current is measured in time [12]. An example of CA can be seen in Figure 7. The current is proportional to the concentration of the analyte, providing the analytical information.

Cyclic voltammetry (CV) is a powerful electrochemical technique used to observe the oxidation and reduction behaviors of a redox species [7]. Figure 8 shows a cyclic voltammogram of a “reversible” redox couple, for instance ferrocenium/ferrocene. The redox reaction between ferrocenium ($Fc^+$) and ferrocene (Fc) can be seen in equation 13, where Cp is a cyclopentadienyl. The CV begins at an initial potential, labeled as A, and moves to a final potential, labeled as D. As the electrode scans more negative, the species at the electrode surface, in this example $Fc^+$, is reduced leading to an increasing current. As the current continues to grow, most of the surface $Fc^+$ has been reduced, and additional $Fc^+$ from the bulk solution is brought to the electrode surface. This slow transport of $Fc^+$ through the so-called diffusion layer results in the eventual decrease of current seen after point C. The reverse occurs in the opposite direction. Fc is converted back into $Fc^+$. The two peak potentials, C and F can be used to determine $E^o$ through the average of both peaks [7]. The peaks and the peak separation seen in a CV are due to the balance between kinetic controlled current (a lower potentials) and diffusion controlled current (at higher potentials). Depending on the peak separation, a reaction is seen as reversible or irreversible. Ideally, a clean electrode with a fast, reversible redox couple, peak separation should be 57 mV/*n*, where *n* is the number of electrons transferred. One negative aspect of the CV is that, due to relatively large charging current, i.e. current due to redistribution of ions instead of Faradaic processes, it is not sensitive enough to detect trace amounts or low surface coverage of adsorbed analyte on an electrode surface.

$$[\mathrm{Fe}\ (Cp)_2]^+ + e^- \rightarrow [\mathrm{Fe}\ (Cp)_2] \tag{13}$$

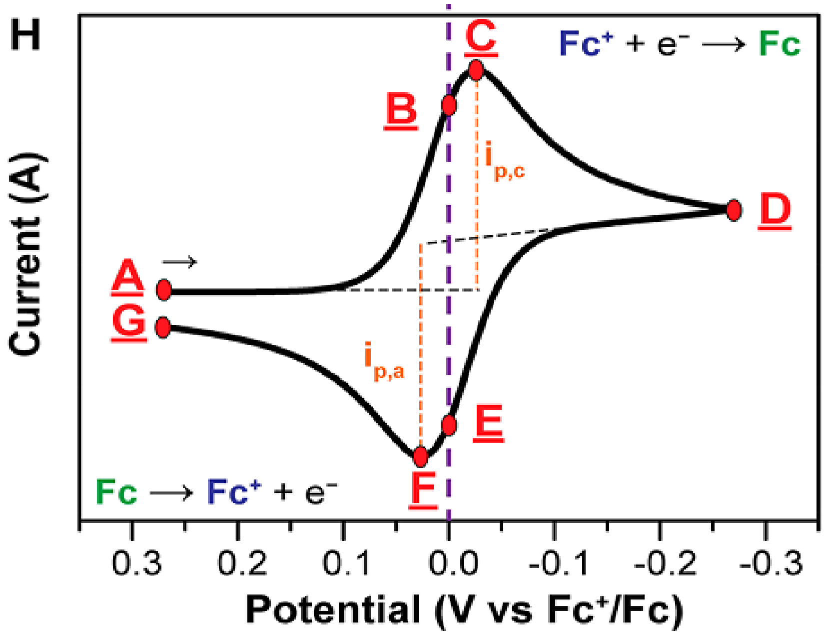

**Figure 8**: A schematic of a cyclic voltammetry waveform [11].

A more sensitive technique to detect trace amounts or surface coverage on an electrode is square wave voltammetry (SWV). SWV superimposes a square wave on a staircase waveform, resulting in the waveform seen in Figure 9 [11]. The SWV is characterized by the pulse size, the distance from the dotted line, as seen in Figure 9, to the top of the square wave and the pulse width, the width of each square wave. The scan begins at an initial voltage and increases the pulse size for pulse width time. At the end of the pulse width time, a current value is measured known as the forward current. The potential then drops down twice the pulse size and scans for the pulse width time. At the end of this time, another current value is measured called the reverse sample. To get the true current value, a difference current is taken, which subtracts the reverse current from the forward current. Once this point is measured, the staircase shifts upward by the step size and repeats this process over again. SWV is often used in DNA biosensors in the presence of a redox tag, such as methylene blue (MB). The quick and sensitive technique of

SWV allows for a clear peak to be shown. The effective scan rates are higher than typically possible using CV. Furthermore, the subtraction of currents effectively reduces the charging current. The peak currents are proportional to concentration, allowing quantitative interpretation.

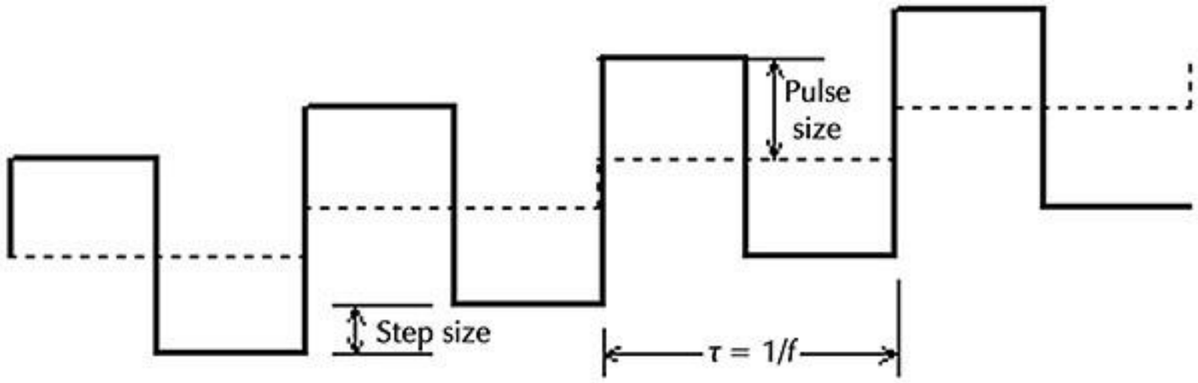

**Figure 9**: A schematic of a square wave voltammetry waveform [11].

The understanding of electrochemistry is essential to understand how biosensors work. Chronoamperometry, cyclic voltammetry and square-wave voltammetry are used in this thesis to detect the chemical and physical properties of DNA as well as drug-DNA interactions. Another important aspect of understanding a DNA biosensor is understanding the structure and replication methods of DNA which will be discussed in the next chapter.

# Chapter 3 Biochemistry of DNA

DNA was first discovered in 1869 by Friedrich Miescher [13]. He was studying the composition of white blood cells and ended up isolating DNA in the process. In 1951, Rosalind Franklin managed to distinguish two forms of DNA strands, A and B form, by using x-ray diffraction [14]. In 1953, Watson and Crick used the research of Friedrich Miescher, Rosalind Franklin, and others to identify the double-helical structure of DNA using diffraction [14]. After the discovery of the double-helical structure of DNA, studies continued to be done on DNA to further explain the function of DNA in the cell and structure of DNA. Many researchers confirmed that DNA consisted of the genetic code of all living organisms. Currently, various fields of study use DNA, such as archeology, forensics, and medicine, to solve and explain specific problems. Due to DNA’s importance, it is imperative to know how the building blocks of DNA fit together, the mechanism of replication of DNA, and how it can be used today in analytical and biosensing applications (including electrochemical approaches) to provide diagnostic information.

## *3.1 Structure of Deoxyribonucleic Acid*

DNA is composed of two linear polynucleotide chains wrapped in a helical structure. Each chain consists of multiple monomers that contain a phosphate group attached to the 5’ carbon of a sugar called deoxyribose [15-16]. These monomers also contain one of four different bases, which include cytosine (C), thymine (T), adenine (A), and guanine (G). The bases attach to the OH group on the 1’carbon through condensation in the deoxyribose. The specific monomer that contains phosphate, deoxyribose, and a base is called a nucleotide. To form a chain of nucleotides, a condensation reaction occurs binding the 3’ hydroxyl group to the previous phosphate group. At neutral pH, the phosphate on the chain has a negative charge. To link two chains together, hydrogen bonding and pi-pi stacking occur between the bases of the nucleotides, overcoming the electrostatic repulsion between the two backbones. Because of the base structure, C and G bind together by three hydrogen bonds while A and T bind by two hydrogen bonds. For these base pairs to bind correctly, they must be antiparallel to one another. C and G are known to be a stronger base-pair interaction than A and T [16]. An example of so-called complementary base pairs can be seen in Figure 10. The binding of these base pairs through hydrogen bonding to form a double-stranded DNA structure is called hybridization [15]. An example of a hybridized DNA structure can be seen in Figure 11.

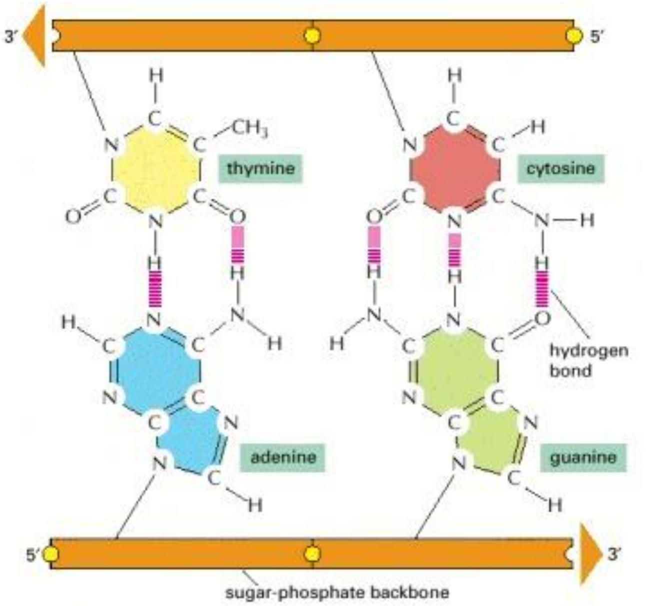

**Figure 10:** An example of the four base pairs. The shape and structure of each base allows the paring of G to C and A to T. Three hydrogen bonds occur between the C to G and two hydrogen bonds occur between the A to T. The DNA strand is typically antiparallel for base pairing to occur. [15]

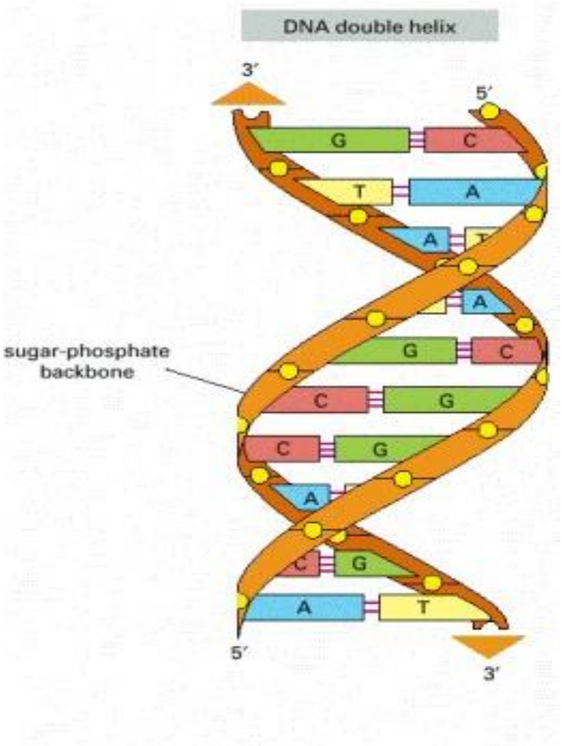

**Figure 11:** The double helical structure of DNA is shown containing the sugar-phosphate backbone and base pairs. When the base pairs bind, hybridization occurs which leads to a double stranded helical structure of DNA to form. [15]

### *3.2 Forms of double-stranded DNA*

There are three main forms of double-stranded DNA: B, A, and Z-form. B-form is the most common type of helical DNA at neutral pH and physiological salt concentrations. It is a right-handed helix and consists of 3.4 nm rise per turn, 10 base pairs (bp) per turn, and a 2 nm diameter [17]. The A-form of DNA is primarily present in RNA-DNA interactions and in RNA-RNA duplexes, as well as dehydrated samples. It is a slightly thicker right-handed helix with a 2.8 nm rise per turn, 11 bp per turn, and 2.3 nm diameter. The Z-form is primarily present when alternating between a purine and a pyrimidine, such as G and C repeating [17]. It is a zigzag formation with a left-handed helix. Because of this zigzag formation, the bp sequence is much more spread out with 22.8 nm rise per turn, 12 bp per turn, and a 1.8 nm diameter. A diagram showing the three different forms can be seen in Figure 12.

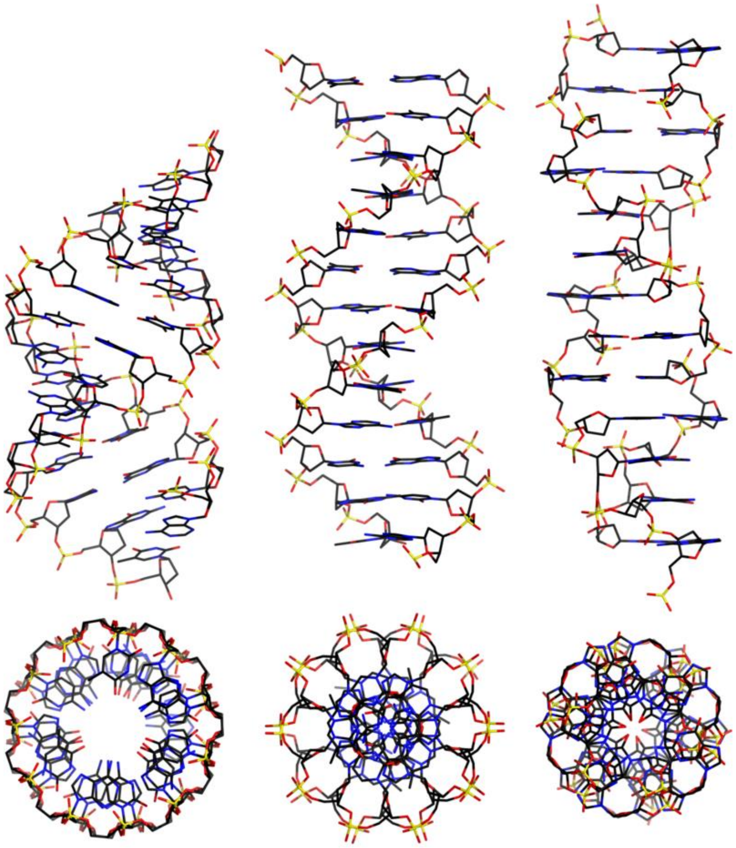

**Figure 12:** The three forms of DNA, B-form (left), A-form (middle), and Z-form (right) [17].

### *3.3 DNA Replication*

DNA provides the genetic instructions to create proteins which are necessary for cellular and bodily function. Proteins are used for transportation within the cell, catalysts for chemical reactions, and muscle formation, amongst other functions. Improper function of proteins can lead to cellular or organism death. DNA mutations often result in proteins that are made improperly during replication. Because the detection of DNA mutations is essential to monitor protein function, it is vital to understand the mechanism of DNA replication and what types of mutations are possible. In this section, an overview of DNA replication is given [18].

DNA replication is the process of copying double-stranded DNA into two identical copies. The first step in DNA replication is the unwinding of the DNA. This is done through an enzyme called helicase, which breaks the hydrogen bonds between the base pairs. While helicase is unwinding the DNA, another enzyme called primase will attach and create a short set of nucleotides called a primer [18]. Starting at the primer, another enzyme, DNA polymerase III, begins to construct the secondary strand. Single-stranded DNA binding proteins (SSB) prevent DNA from hybridizing once separate. There are two different strands the DNA polymerase III can bind to; the leading strand and the lagging strand. The leading strand is synthesized in the 5' to 3' direction and the DNA is synthesized toward the replication fork. The lagging strand is synthesized in the 3'to 5' direction and the DNA is synthesized away from the replication fork. Depending on which strand DNA polymerase binds to, it will behave differently. On the leading strand, DNA polymerase III will go through the stand with no stops. On the lagging strand, since DNA is being replicated in the reverse direction of the replication fork, the DNA polymerase does not go continuously but creates Okazaki fragments [18]. Once these fragments are made, they are sealed together by DNA ligase, creating a continuous strand. A diagram illustrating DNA replication can be seen in Figure 13.

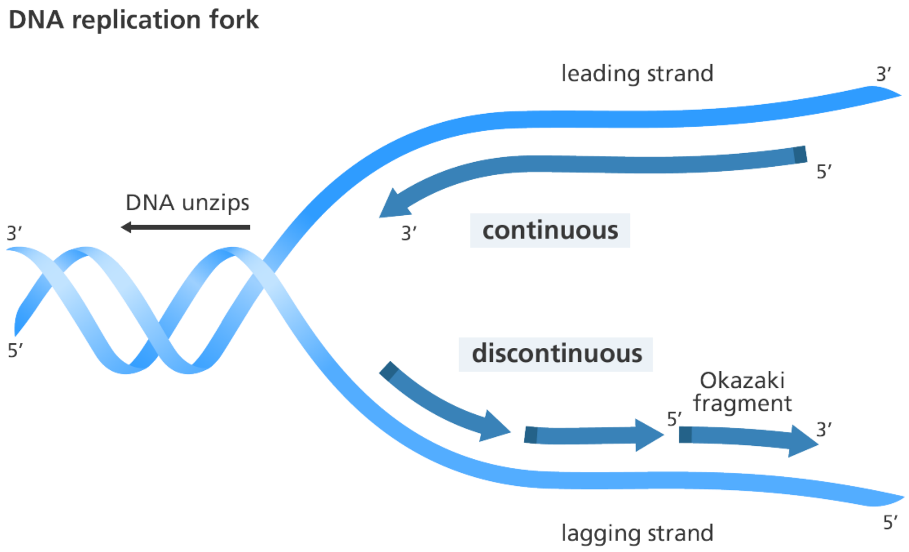

**Figure 13:** An example of DNA replication is shown. DNA unzips through helicase. Once a primer is attached, DNA polymerase constructs the complementary sequence of DNA on both the leading and lagging strand. [19]

Sometimes, genetic mutations can occur during DNA replication leading to the change in base-pair sequences. Genetic mutations can have minimal, dramatic, or no effect of the function of the proteins created. An insertion mutation is defined by an addition of a nucleotide during replication. This type of mutation shifts the open reading frame of the sequence leading to a different or nonexistent amino acid formation. A deletion mutation removes a set number of nucleotides during replication which shifts all nucleotides downstream. Finally, a nonsense mutation changes one base pair which leads to a stop codon during amino acid formation mid-stream [20].

### *3.4 Polymerase Chain Reaction*

Methods based on polymerase chain reactions (PCR) are routinely utilized in genetics and molecular biology to amplify DNA and RNA fragments. Various fields have applied PCR, including forensics, diagnosis of heredity diseases, and DNA sequencing [21-22]. Amplification of DNA using PCR occurs in 3 steps: denaturation, annealing, and elongation. These three steps are repeated 20-40 times, resulting in $2^n$ copies of DNA where n is the number of cycles [22]. Figure 14 summarizes the three steps of PCR.

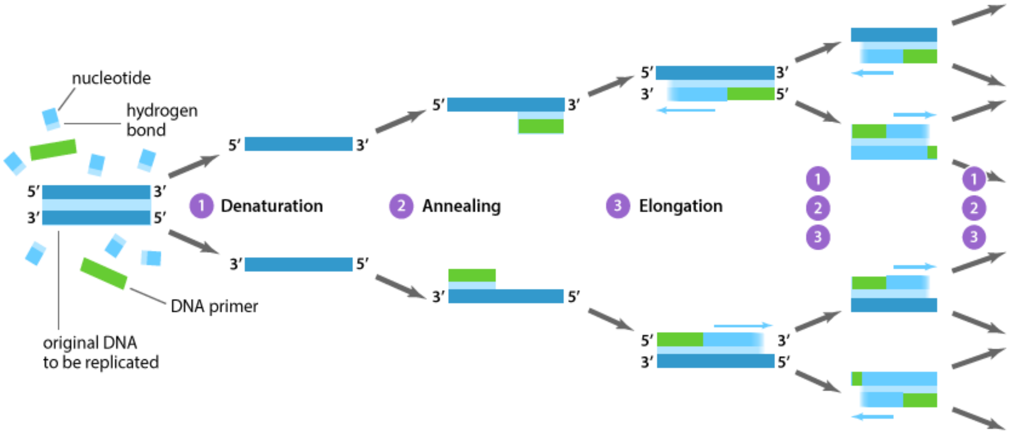

**Figure 14:** PCR can be summarized in three steps: denaturation, annealing and elongation. 1) Denaturation allows for DNA to completely melt. 2) annealing attaches the primer 3) DNA polymerase creates the complementary strand of DNA. Each cycle, the amount of DNA is increased by $2^n$. [22]

First, a reaction vessel containing primers, deoxyribose nucleotide triphosphate, dNTP, DNA polymerase, and double-stranded DNA (dsDNA) is heated at 95 °C for 5 minutes. This heating allows for activation of the polymerase, denaturation of any contaminants, and lysing of cells to release the dsDNA [21]. During the denaturation step, the vessel is heated at 95 °C for 8 minutes. Thus, allowing hydrogen bonds to be broken between the strands of DNA, resulting in the melting of the dsDNA into single stranded DNA (ssDNA). Next, during the annealing step, the temperature is lowered to between 50 °C and 65 °C and a primer is attached to the ssDNA. A primer is a small segment of DNA that DNA polymerase III attaches to create the complementary strand of DNA. The temperature is lowered to create ideal conditions for the annealing of the primer. If the temperature is too high, the primer will not anneal or attach. If it is too low, non-specific binding will occur, and the primer will not duplicate the section of DNA to which it is targeted. Primers are often in large excess to favor hybridization over reannealing of the dsDNA. In the last step, elongation, DNA polymerase binds to the primer and uses deoxyribonucleoside triphosphate (dNTP) to create a complementary strand to the primer and DNA. The temperature during elongation depends on the heat resistance of DNA polymerase and is usually around 72 °C. The time of elongation depends on the length of the DNA strand and the speed of the DNA polymerase. DNA polymerase typically run at about 1.5kb/min. This means that there are 1.5 kilobase pairs are copied per minute at optimal temperatures [22]. After the aliquoted amount of cycles has been reached, final elongation is done at 75 °C for 10 minutes to ensure all DNA strands have been fully elongated. Short-term storage is done between 4-15 °C.

In a typical PCR reaction, DNA will continue to increase by $2^n$ (where n is the number of iterations of PCR) until all the substrates have been used or the user stops the reaction. However, DNA does not extend at this rate for all cycles. The PCR reaction occurs in three phases, exponential, linear, and plateau phases [23]. In the exponential phase, DNA doubles after each period. After a certain amount of time, the PCR reaction will enter the linear phase or the non-exponential phase. During this phase, DNA duplication slows down and no longer increases exponentially. This primarily occurs because of increased competition of the reannealing of dsDNA and annealing of the primer and the rates of specific components being depleted. Eventually, the PCR reaction runs out of resources to continue and enters the plateau phase. These different phases are shown in Figure 15 [23].

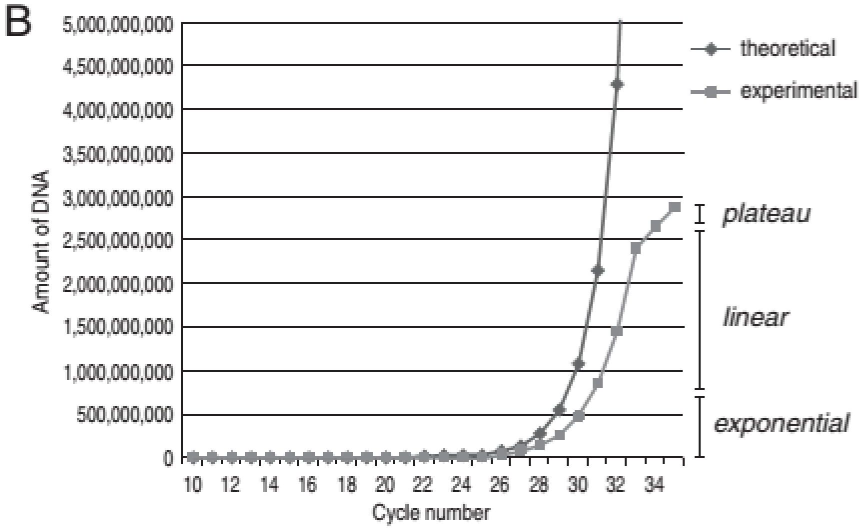

**Figure 15:** In PCR, the amount of DNA is predicted to increase exponentially until the no more reagents are available, as shown in the theoretical line. It is observed in the experimental line that due to competition between the primer and reannealing DNA, and depletion of resources at different times, the amount of DNA does not continue exponentially for the full length of the reaction. [23]

Once DNA is duplicated, various other tests need to be done to verify that the target DNA is present and has been duplicated. These may include high performance liquid chromatography (HPLC), gel electrophoresis, or capillary electrophoresis [19]. These extra processing methods can make PCR unfavorable for some application due to lack of automation, high costs, reprocessing steps, and false positives [21]. False positives primarily occur due to amplification of contaminating nucleic acid sequences. To minimize error from reprocessing and increase efficiency, an improvement of PCR was created called quantitative PCR (qPCR).

### *3.5 qPCR*

Quantitative polymerase chain reactions (qPCR), also known as real-time polymerase chain reactions, includes a method to quantify the amount of DNA present with minimal post-processing. The first generation of qPCR utilized a florescent dye in the PCR mix. The fluorescent dye was chosen for its ability to bind to the hydrophobic region of double-stranded DNA between base pairs. The signal is directly proportional to the amount of DNA present. Originally ethidium bromide (EtBr) was the primary dye used in qPCR. The fluorescence intensity of ethidium bromide is dependent upon how much is bound to the DNA. Free EtBr has the lowest fluorescent signal whereas EtBr bound to ssDNA is higher and EtBr bound to dsDNA is the highest [21]. As qPCR takes place, the ethidium bromide binds to the new dsDNA and the fluorescent signal increases. Once the reaction is complete, most of free EtBr dye will be bound to dsDNA. While some of the EtBr will bind to ssDNA, the binding efficiency is much less, and the signal is assumed to be the signal of just EtBr-dsDNA. The fluorescence can be measured before, during, or after the PCR reaction [21]. A more common type of dye used in qPCR is SYBR Green I due to it having an affinity 100 times larger than ethidium bromide to dsDNA and having a low cost [21,24]. SYBR Green is also favorable for having a strong emission signal at 520 nm that becomes 1000 times stronger when bound to dsDNA versus free dye [21]. Figure 16 illustrates SYBR Green I binding to dsDNA during qPCR. Although SYBR Green I is highly effective at binding dsDNA and provides a strong signal, it also has its downside in qPCR. For example, it has been observed that SYBR Green I can inhibit PCR elongation, affects DNA melting temperature, and in some cases lacks adequate specificity for dsDNA [23-25].

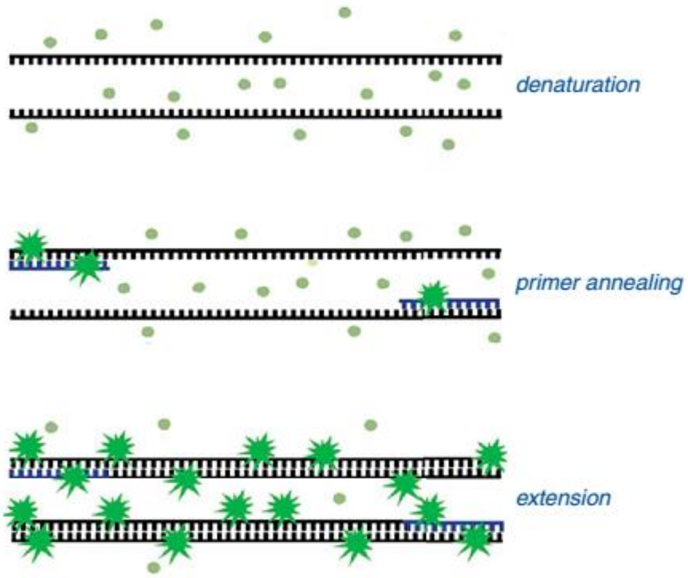

**Figure 16:** When SYBR Green binds to dsDNA, it has a fluorescent increase 1000 times more than unbounded dye. Signal increase is detected during the elongation step [25].

PCR can also be used as a diagnostic tool to detect foreign substances in the body. Safeukui et al. recently developed a method using PCR to detect different strands of parasites that cause malaria [26]. Safeukui worked with four different parasites that cause malaria, *P. falciparum, P.vivax, P.ovale, and P.malariae*. A probe sequence was developed by taking advantage of a mismatch that is present on the *P. falciparum* versus the other three sequences. The probe was also labeled with a fluorescein isothiocyanate (FITC) at the 5’ end of the DNA sequence. The type quantification of PCR used in this experiment is fluorescence resonance energy transfer (FRET) [26]. The FRET signal was used in parallel with melting. FRET was done on three different samples of blood and one control to see if FRET could distinguish between parasites. The results of this can be seen in Figure 17.

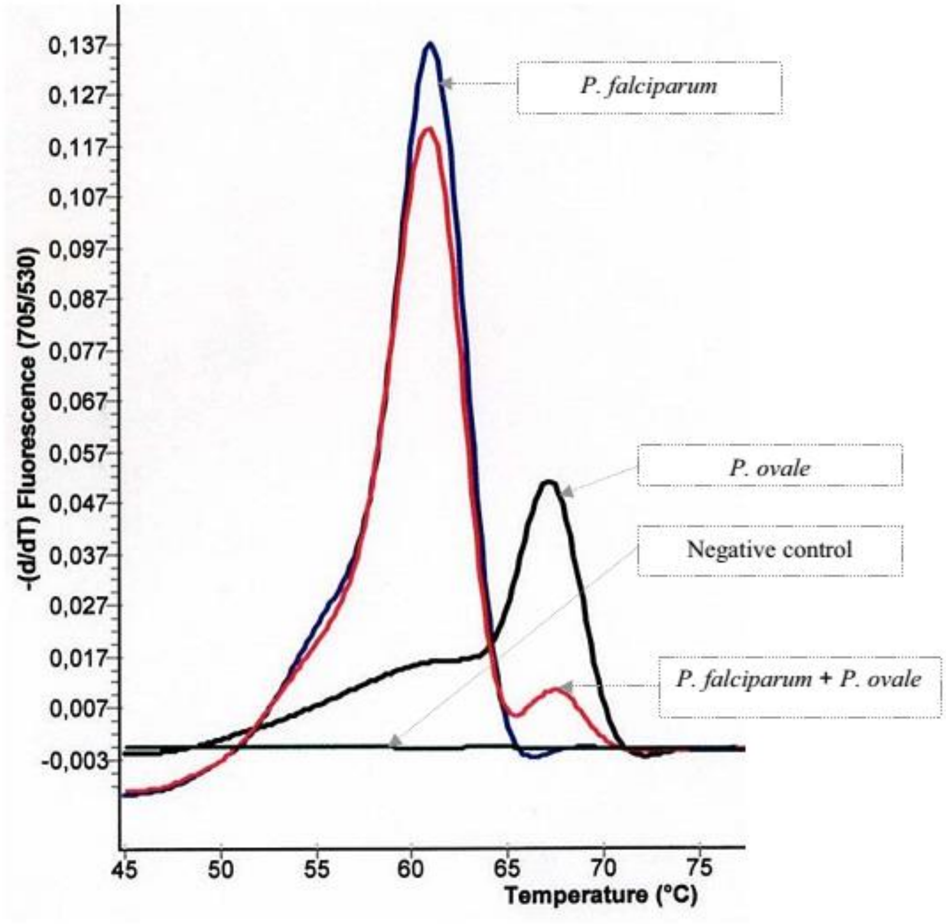

**Figure 17:** Four melting curves are shown using three different blood samples. The three blood samples were *P. falciparum, P. ovale,* and *P. falciparum + P. ovale*. The negative control that was run consisted of the reaction mixture with water [26].

Through these results, it can be concluded that not only can PCR detect the different strands of parasite present, it can also distinguish between blood samples that have multiple types of parasites. The use of FRET fixes a common problem that SYBR Green I has, in that it allows the specificity of DNA strand to be shown.

### *3.6 Biosensors and qPCR*

While various forms of PCR exist, and are powerful tools for genetic analysis, DNA biosensors are promising for applications where benchtop equipment and long analysis times are not ideal, e.g. point-of-care diagnosis and monitoring. Biosensors have the potential to be cheaper, faster, and more portable. Biosensors rely on specific interactions between a recognition element and the target, followed by transduction to an electrical signal, often employing optical, gravimetric or electrochemical detection. Electrochemical detection is particularly promising due to the minimal electronics, miniaturization, ability to multiplex, and fast measurement times. Often in qPCR, small molecules of microRNA (miRNA) are used. miRNA is a small nucleotide sequence, around 22-nucleotides, whose primary goal is to regulate gene expression. Due to its small size, finding a flexible primer for miRNA is difficult [21]. Furthermore, miRNA lacks specificity in qPCR meaning the sample must be free of any other RNA or DNA sequences and denaturing agents that could negatively affect polymerases such as inhibitors. A DNA electrochemical biosensor can potential avoid these and other drawbacks of benchtop techniques [28].

For example, the principle of one electrochemical DNA biosensor is illustrated in Figure 18 [29]. A gold electrode is used and a layer of thiolated DNA acts as a probe for miRNA to hybridize with. Thioglycolic acid is then used to fill any remaining gaps on the monolayer. Once miRNA has been added duplex specific nuclease (DSN), removes DNA and miRNA duplexes. DSN has been shown to selectively cleave DNA-DNA interactions (duplexes) and DNA-RNA duplexes and not RNA-RNA duplexes. The miRNA is recycled and reattaches to another strand of DNA probe which is then removed by DSN. This cycle continues until all DNA probe is removed by DSN. An electrochemical impedance spectroscopic test, EIS, is preformed using

$Fe(CN)_6^{4-}$ and $Fe(CN)_6^{3-}$ redox probes to determine the amount of miRNA present in the original sample. This method can detect miRNA as low as 1.0 fM, or 1 $\times 10^{-15}$ M [29]. While this particular approach still relied on miRNA, it illustrates the potential for adaptation of existing methodology towards development of DNA biosensors.

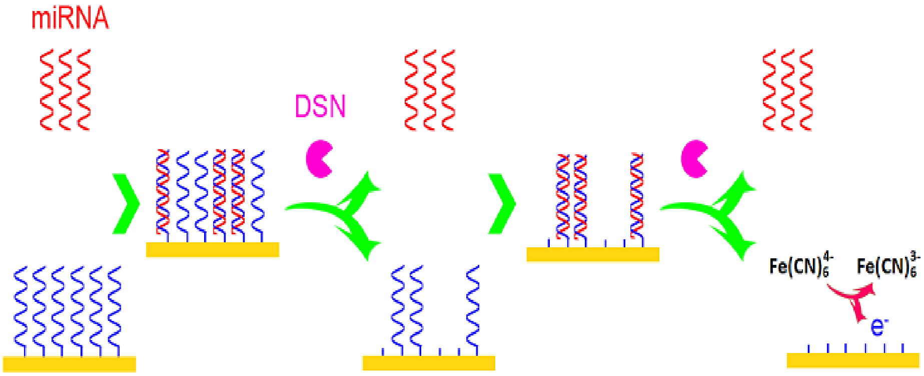

**Figure 18:** An alternative method to detect miRNA other than qPCR is the use of an electrochemical biosensor. miRNA hybridizes with probe DNA and is cleaved by DSN. miRNA is reused and the process is repeated. EIS is performed to determine the concentration of miRNA present. [29]

Rather than remove qPCR completely, another method is to combine electrochemical sensors with qPCR. This method is called electrochemical real-time polymerase chain reaction or ERT-PCR. ERT-PCR is typically carried out on an integrated silicon chip, which allows qPCR and electrochemical detection to be done simultaneously on the same device. Figure 19 shows both a glass chip and a silicon chip set-up for ERT-PCR. For ERT-PCR to work correctly, it must fulfill all the requirements of qPCR, i.e., thermal stability and no PCR inhibition. To do this, a platinum (Pt) temperature sensor and heater is incorporated in the chip to allow for proper thermal cycling. A Pt electrode patterned in the silicon acts as the working electrode. Also, on the chip is a PCR chamber. A DNA blank probe is incubated in the chamber overnight. Next, the master mix is added, consisting of reaction buffer, dNTP, forward primer, reverse primer, and DNA polymerase and Fe-dUTP. Fe-dUTP is a labeled nucleotide that can show the progress of qPCR. A total of 30 cycles of qPCR is carried out followed by voltammetric measurements [30].

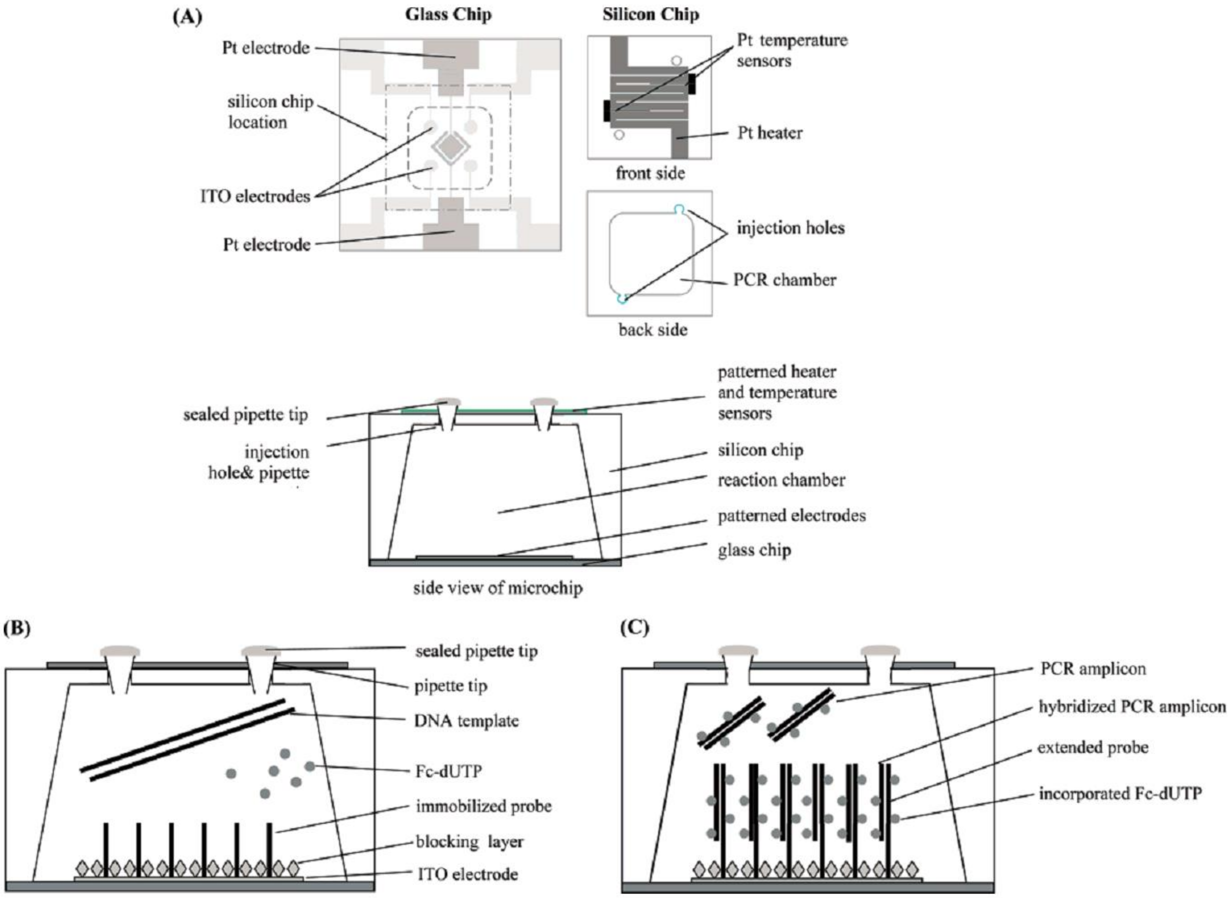

**Figure 19:** A) Shows the front, back and side view of the silicon chip. B) shows the PCR chamber before PCR begins and C) shows the PCR chamber after PCR is completed. [30]

Other electrochemical biosensing approaches use PCR in conjunction with subsequent detection via electrochemical measurement. In these cases, the PCR step is used to amplify the target. In Bartlett's et al. research, two different bacteria were analyzed: *Yersinia pestis*, one of the main causing bacteria of the plague, and its closely related species *Y. pseudotuberculosis* [31]. To do this experiment, a gold surface was modified with a thiol probe and a passivation layer consisting of mercaptohexanol. The probe was then hybridized with the target sequence previously amplified using PCR. A dye, Texas Red, was used as a surface enhanced Raman indicator for this experiment. Surface-enhanced Raman spectroscopy (SERS) was used to analyze the melting behavior of each sequence as the electrode potential is scanned in the negative direction, causing electrostatic repulsion on the negatively-charged DNA backbone and the electrode surface. This method of melting DNA is known as electrochemical melting, electrostatic denaturation, or electric field-assisted dehybridization. A summary of the results can be seen in Figure 20 [31]. DNA sequences were taken from two different genes *groEL* and *metH* of the two bacteria species. Once hybridization occurred, the sequence was melted. Using PCR, the target sequence can be in large enough concentration to hybridize with the probe. DNA melting can then be used to distinguish between the two different bacteria in two different genes. Electrostatic denaturation is the focus of the work in this thesis, and will be discussed more later.

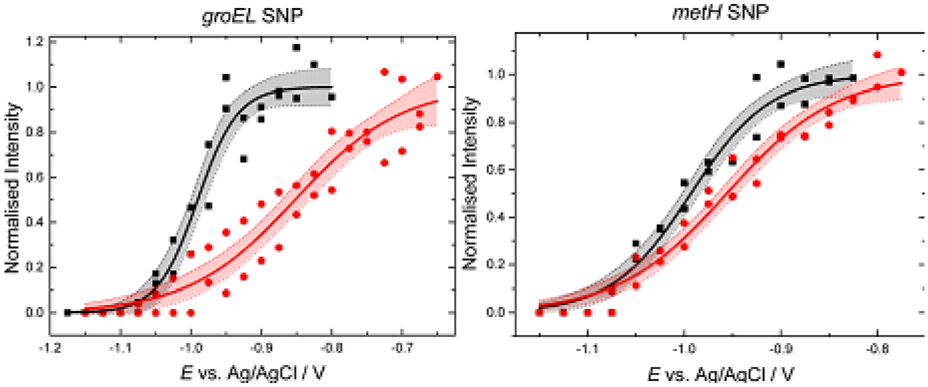

**Figure 20:** Melt curves are shown obtained by SERS. *groEL* and *metH* genes were targeted. The black data represents the DNA from *Y. pestis* and the red data represents the data from *Y. pseudotuberculosis.* The samples can be distinguished based on melting curve.[31]

Due to the importance, and sometimes low concentration of DNA in biological samples, methods of DNA replication and amplified detection methods are often needed. PCR and qPCR provide excellent methods to amplify DNA. Combining PCR with techniques such as fluorescence or electrochemical techniques provide a method to further analyze DNA. It has been shown that if a high enough concentration of DNA is present, different strands of DNA can be distinguished. Better yet, would be a biosensor with enough inherent amplification so that PCR would not be necessary.

# Chapter 4 Optimization of DNA Electrodes

## Introduction

The development of DNA biosensors is an active area of research due to its practical use in medicine, forensics and detection of biomarkers [32]. In many of these sensors, and our research, a gold substrate is used due to facile chemistry with thiol-modified DNA, allowing monolayer formation. The gold biosensor is first modified with a mix of modified ssDNA called probe and a passivating layer such as mercaptohexanol. This modified probe with a thiol allows for easy chemisorption to the gold surface. The complementary strand is then added with an optical or redox tag that results in a measurable signal. This complementary strand is called the target. In the work presented here, we obtain additional information about the hybridized DNA by electrostatic denaturation. A constant negative potential is applied to the gold, and the phosphate backbone of the DNA is repulsed from the electrode. While the probe strand is covalently tethered, the target strand can unzip from the probe and leave the electrode surface, i.e. the DNA helix melts. As the redox tag leaves the surface, measured signal decreases. Throughout the experiment, SWV is used to measure the reduction of the redox tag, methylene blue (MB). In this chapter, optimization of the melting process, and the electrode modification procedure is presented. Additionally, the effects of DNA density and ionic strength are explored.

### *4.1 Previous Research*

Previous work in our lab showed that electrostatic denaturation can be used to detect useful information such as the presence of a single mismatch, the presence of a hairpin, and even differences in oligonucleotide length [32]. In thatwork, the effect of melting potential was explored, and both constant potential and scanning potential melts were carried out. More negative potentials resulted in faster melting, and potentials more positive of ~-300 mV resulted in negligible melting. It was found that using a constant potential of -500 mV minimized thiol desorption, which can occur as the thiol bond is reduced at sufficiently negative potentials. While comparison of melts at -500 mV allowed discrimination of DNA based on, e.g. presence of mismatches, the standard deviation in the surface coverage (and therefore signal) was quite high. The goal of the studies presented in this chapter was to improve the reproducibility of these measurements by improving the electrode modification procedure. Furthermore, preliminary results are presented on the effect of ionic strength and DNA surface coverage, with the goal of finding conditions which will improve the reproducibility of the melts.

## *4.2 Materials*

All chemicals were purchased from Sigma-Aldrich and used as received. The modified oligonucleotides used in this work were purified by dual high-performance liquid chromatography (LGC Biosearch Technologies, Petaluma, CA). Both probe and target sequences contain 18 base pairs and are fully complementary with each other. The DNA strands used can be seen in Table 1.

**Table 1:** Table of DNA.

| | |
|---|---|
| *18-bp Duplex (**MB** on target)* | Probe: 5’HS-C6-TTG ATC GGC GTT TTA TTC 3’<br>Target: 3’ (MB)-AAC TAG CCG CAA AAT AAG 5’ |
| *18-bp Duplex (**MB** on probe)* | Probe: 5’HS-C6-TT(MB)G ATC GGC GTT TTA TTC 3’<br>Target: 3’ AA----C TAG CCG CAA AAT AAG 5’ |

Solutions of 6-mercapto-1-hexanol (MCH) and thiolated probe DNA were prepared in 10 mM phosphate buffer containing 2.7 mM KCl and 1.14 M NaCl (pH 7). Hybridization of surface-bound probe and target was carried out in 10 mM Tris containing 1 M NaCl and 1 mM EDTA (pH 7). Electrochemical melting was performed in 10 mM Tris buffer (pH 7), and electrodes were rinsed in 5 mM Tris buffer containing 10 mM NaCl (pH 7). All solutions were prepared using deionized water.

All electrochemical experiments were carried out using polycrystalline gold disk working electrodes (geometric surface area 0.0314 $cm^2$ and roughness factor ca. 1.4), Ag/AgCl (1 M KCl) reference electrode, and platinum wire counter electrode (CH instruments, Austin, TX). Electrochemical melting was carried out using a VersaStat 4 potentiostat and VersaStudio software (Ametek Scientific Instruments, Berwyn, PA) at a temperature of 30 °C. Electrochemical polishing was carried out on either a VersaStat 4 or a WaveNow (Pine Research, Durham, NC) potentiostat.

### *4.3 Methods*

Gold electrodes (2 mm diameter, CH Instruments, Austin, TX) were cleaned using a three-step process. The electrodes were first mechanically polished using a 0.05-micron alumina slurry for 2 minutes then sonicated in deionized water for 5 minutes. The gold electrodes were then cleaned chemically with a piranha solution: 3:1 concentrated sulfuric acid to 30% hydrogen peroxide, for 40 seconds

[CAUTION]: Piranha is highly corrosive and its acidic vapors cause a severe inhalation hazard which can be destructive to the mucosal membranes and result in severe burns. Skin or eye exposure to piranha solution can cause severe burns].

After thoroughly rinsing the electrodes with deionized water, they were electrochemically cleaned in a 0.5 M sulfuric acid solution. This polishing process consists of (1) using cyclic voltammetry between -0.2 to 1.6 V for 50 cycles at 10 V/s and (2) -0.2 V to 1.6 V for 10 cycles at 50 mV/s. The electrodes were then rinsed and stored dry until further use.

Tris(2-carboxyethyl)-phosphine-HCl (TCEP) was used to reduce the disulfide bond of the probe. A DNA probe solution was then made at 0.5 μM and pulsed from 0.5 V to -0.2 V at room temperature at 10 ms intervals for 15 minutes. Electrodes were then rinsed and stored overnight in a 9 mM MCH in PBS buffer at 4 ° C. After the attachment of probe and MCH, the electrodes were rinsed and placed in 60 μL of tagged MB target for 40 minutes. A summary of the modification process can be seen in Figure 21.

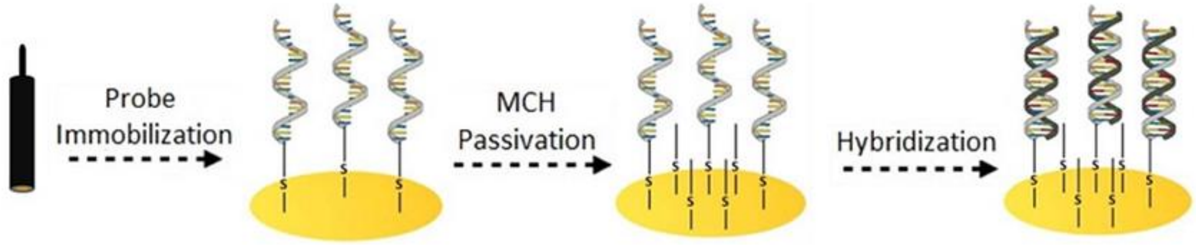

**Figure 21:** A clean gold electrode is used to pulse probe and attach MCH. Then the tagged target is hybridized to the complementary strand. [32]

### *4.3.1 Electrostatic Denaturation Routine*

The electrochemical melting routine consists of programmed potential pulses used to melt the DNA. First, the electrode is allowed to equilibrate at open cell potential (OCP) for 10 minutes. Next, chronoamperometry is used to apply a constant potential of -500 mV (vs. Ag/AgCl in 1 M KCl) for 8 minutes. This negative potential repels the negatively charged phosphate backbone of the DNA resulting in dehybridization. Next, -0.1 V is applied for 10 s. This step allows equilibration of the electrode. Finally, SWV is done to monitor the amount of target DNA still bound via reduction of the pendant methylene blue label. The voltammogram is acquired using the following parameters: initial potential of -0.1 V, final potential of -0.45V, amplitude of 25 mV, period 6 ms and increment of 5 mV. Once the SWV is done, the cycle is repeated starting at the -500 mV melting step. The cycle is repeated 10 times. The full potential waveform applied during the melt is depicted in in Figure 22.

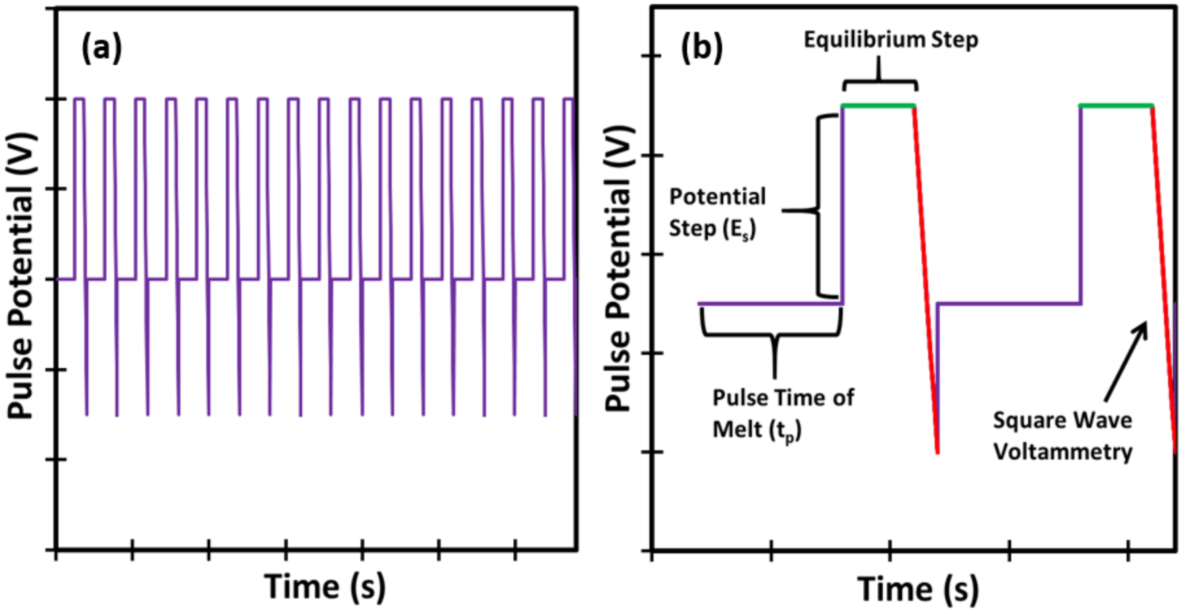

**Figure 22:** The potential waveform applied during electrostatic denaturation at constant potential. (a) 17 cycles are shown comparing the pulse potential to time. (b) One cycle is shown. After the open cell potential (not shown here) the electrode is set at a constant potential of -500 mV for 8 minutes represented by $t_p$ (purple line in b). The potential is then brought up to -100 mV for 10 s (green line in b), $E_s$ before a SWV is acquired (red line in b).

After the completion of the melt, voltammograms were used to analyze overall melting. The voltammograms were baseline-subtracted, normalized to the initial signal, and plotted versus time to obtain a kinetic melting curve. An example of the SWVs obtained during a melt can be seen in Figure 23, and a kinetic melting curve produced from this data can be seen in Figure 24. The kinetic melting curves are fit with the following equation:

$$i_p(t) = \boldsymbol{A}e^{-t/\tau} + (1 - \boldsymbol{A}) \tag{14}$$

Where $\tau$ is the *time constant* and $A$ is the *melting extent*. These fitting parameters provide insight into the kinetics and thermodynamics of the melting process, and ultimately the stability of the dsDNA. A slower melt will have a larger *time constant* while a faster melt will have a smaller *time constant*.

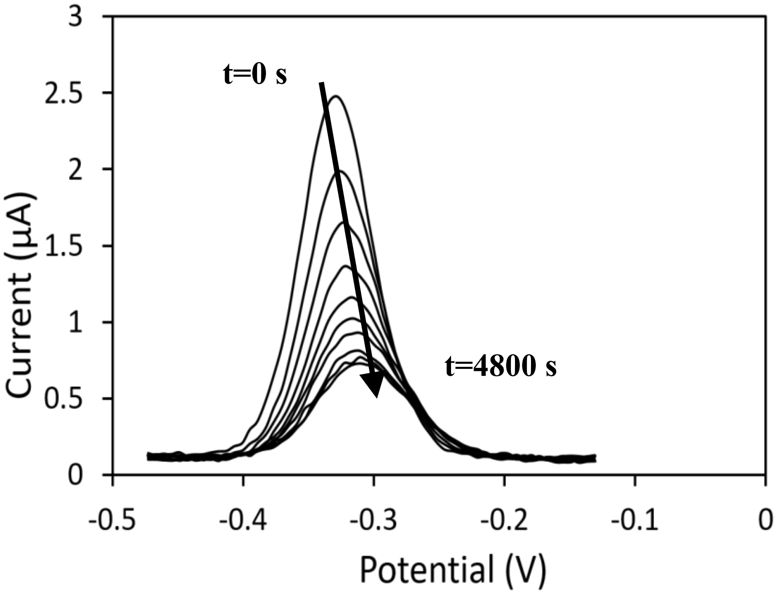

**Figure 23:** Voltammograms collected during a melt. As the melt progresses, since MB is no longer near the surface, the voltammogram current decreases over time. Experiments are done in 10 mM Tris buffer at pH 7. Voltammograms are run at an initial potential of -100 mV and a final potential at -450 mV.

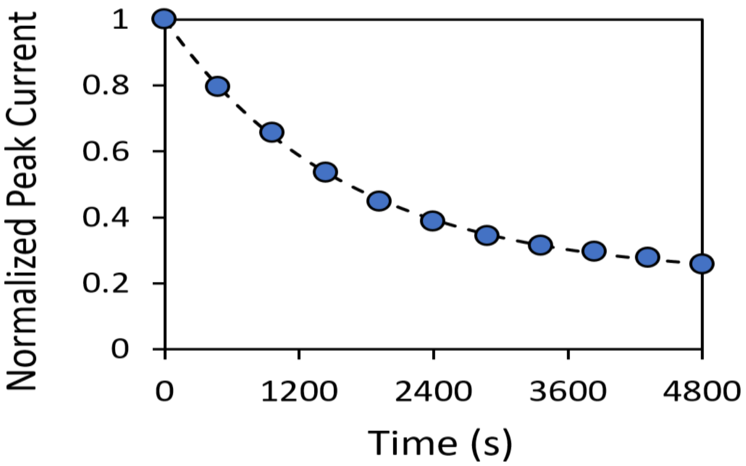

**Figure 24:** To analyze each voltammogram, the each SWV is normalized to the initial voltammogram peak height and plotted versus time. Using equation 14, the *time constant* and *melting extent* are determined.

To determine the surface density of probe on the electrodes, a chronocoulometric hexaammineruthenium (III) chloride (RuHex) assay was implemented [33]. A MB-tagged probe solution was pulsed on gold electrodes and incubated in a 9 mM MCH solution overnight. A potential was applied to the electrode in a 50 μM of RuHex with 10 mM Tris Base. Before running, the solution was degassed for 10 minutes using inert argon gas. The experimental parameters consisted of an initial potential of 0.1 V for 2 seconds followed by a final potential of -0.4 V for 1 second at room temperature [33]. The results of the assay were then analyzed to determine the number of DNA molecules per $cm^2$.

## Results and Discussion

### *4.4 Optimization of Probe Density*

In our lab, the probe has traditionally been adsorbed to the gold electrode through passive methods. This was done by taking a clean gold electrode and incubating it in a 10 μM solution of probe overnight at 4 $^{o}$C. The next day, the electrode was rinsed and placed in a 9 mM MCH solution for 1 hour to form a passivation layer. Finally, the electrodes were placed in a solution of 5 µM MB tagged target for 2 hours at room temperature in the dark. This procedure often resulted in inconsistent peak heights and consequently a variable melting behavior. To address this issue, a potential pulsing technique was implemented for better control over chemisorption of the probe. This technique involves pulsing from a high potential, 0.5 V, to a low potential, 0.1 V at a fast interval, 10 ms at each potential in a solution of the probe. This rapid change results in an "ionic stirring effect" which helps facilitate diffusion of the probe to the electrode surface. This "ionic stirring effect" has been shown to increase the consistency of probe attaching to the gold surface and shorten the time to do so [34-35]. A portion of the pulsing waveform can be seen in Figure 25.

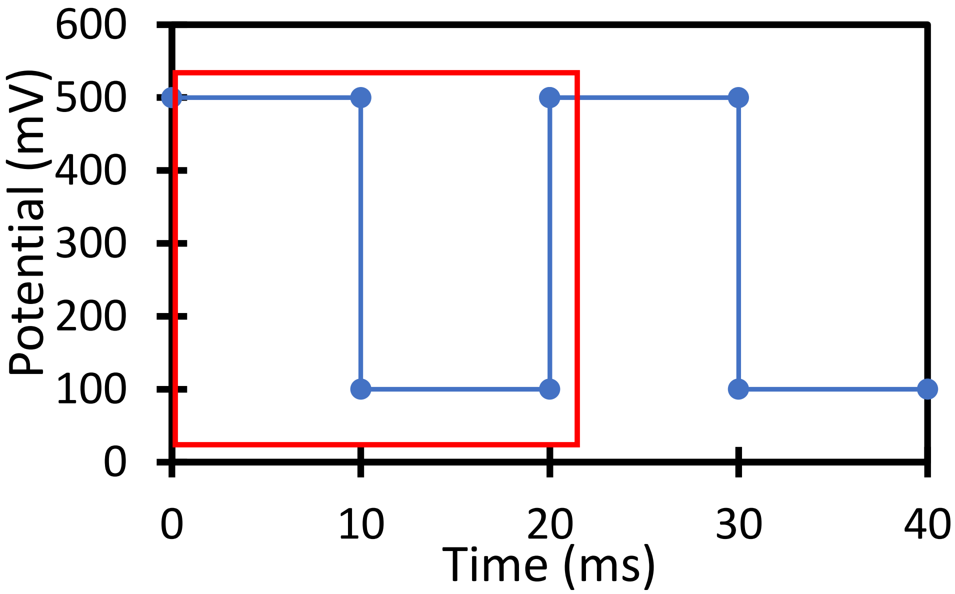

**Figure 25:** The potential pulse routine used for improved pulse chemisorption. The pulsing routine starts at + 500 mV for 10 ms followed by +100 mV for 10 ms. The red box represents one cycle of this routine.

Two experimental variables were adjusted to test the effectiveness of the pulsing technique for obtaining monolayers with consistent and controllable surface densities: total pulsing time and concentration of DNA. First, each electrode was pulsed using tagged probe at 0.5 µM (under the previous stated conditions) for 5, 10 or 15 minutes respectively. A RuHex assay was then carried out to estimate the surface coverage. The results shown in Figure 26 reveal that when the pulse time was increased, the surface density of probe increased. Tarlov et al. were only able to obtain 8 x $10^{12}$ molecules per $cm^2$ using passive methods [33]. At 15 minutes of pulsing, a value of 1.2 x $10^{13}$ molecules per $cm^2$ is obtained. This larger density

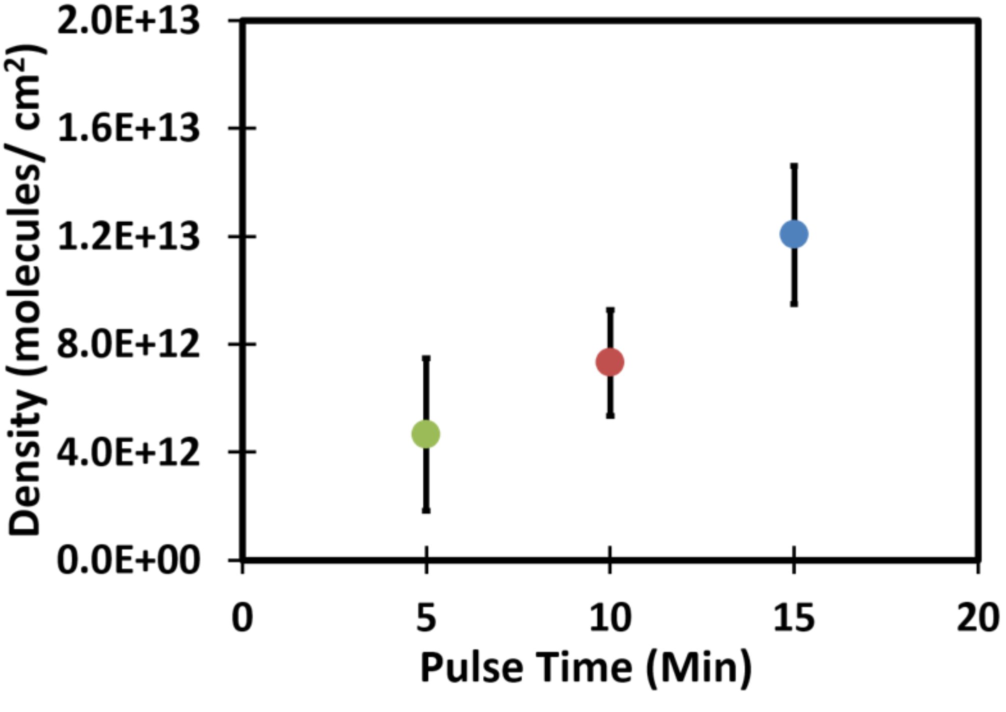

**Figure 26:** Pulse time as compared to density using the RuHex assay. As pulse time increases, the density of probe on the electrode increase.

shows that a higher surface coverage can be obtained using the pulse assisted method in a shorter amount of time.

A similar experiment was done to explore the effect of probe concentration. Because 15 minutes gave the highest probe density of the three tested (see Figure 26), this was the pulse time used when exploring the effect of probe concentration. Electrodes were pulsed for 15 minutes at the following concentrations, 0.0625, 0.125, 0.5 and 1 μM. Again, the RuHex assay was used to quantitate the surface coverage. The results can be seen in Figure 27. As the concentration of probe increases, the surface density increases in a non-linear fashion. Beyond 0.5 μM, the surface density appears to flatten out as steric and electrostatic hinderance are expected to inhibit chemisorption of the probe [33].

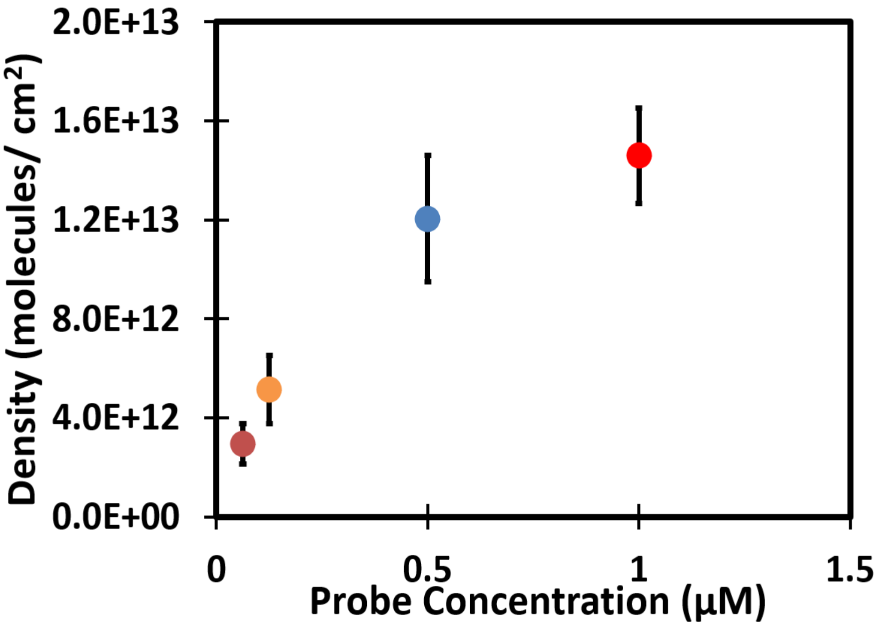

**Figure 27:** Density of probe is related to probe concentration. Given a constant pulsing time, as probe concentration increases, the surface density increases until it flattens out at some point beyond 0.5 μM.

While the RuHex test provides a direct electrochemical method for quantifying surface coverage, the complexity and time required do not allow it to be used during the electrochemical melting routine itself. Also, RuHex has a high affinity for the DNA backbone, and its reduction peak overlaps with that of methylene blue, thus complicating data analysis. Therefore, a method is needed to compare the surface coverage obtained from the RuHex test to the MB signal obtained. To do this, a voltammogram was taken of the tagged MB probe at four different concentrations 1 μM, 0.5 μM, 0.125 μM, and 0.0625 μM pulsed one time for 15 minutes. The peak currents obtained were then compared to the peak currents obtained during the use of the passive method. The results of these measurements can be seen in Figure 28.

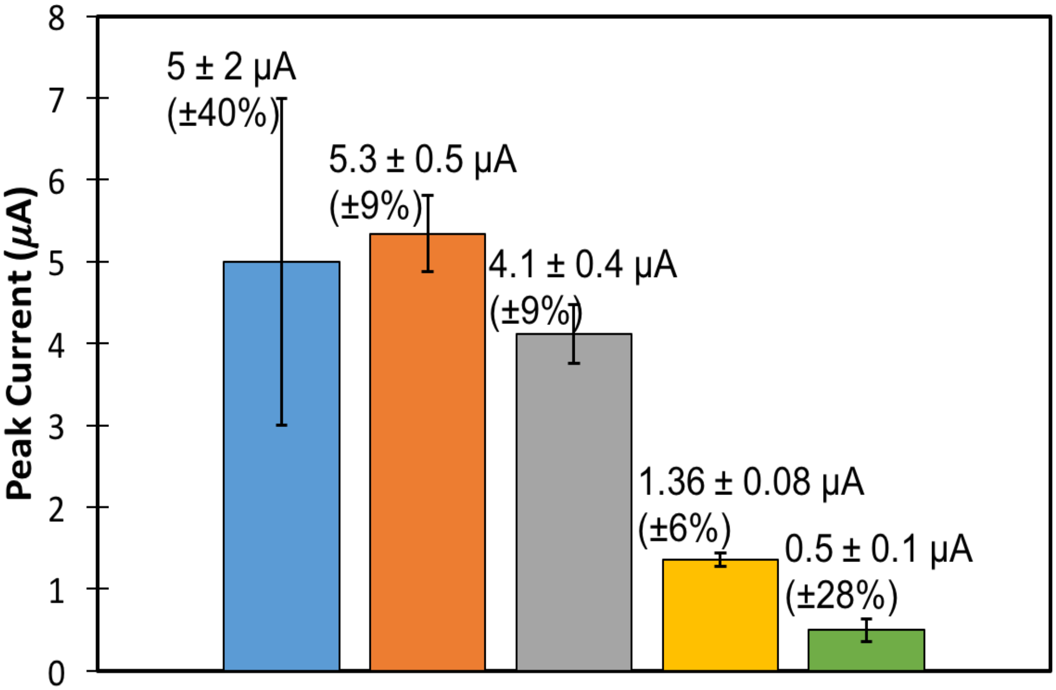

**Figure 28:** Comparison of passive and pulse assisted probe chemisorption. The blue bar is passive chemisorption of probe from 10 μM probe. Pulse assisted probe (15 minutes) is shown for comparison at 1 μM, 0.5 μM, 0.125 μM, and 0.0625 μM probe in orange, grey, yellow and green respectively. The error bars show the standard deviation of triplicate measurements, clearly illustrating the improved reproducibility introduced by the pulsing.

Previous studies by Tarlov et al. used passive probe chemisorption resulting in a maximum surface coverage of around 8 x $10^{12}$ molecules per $cm^2$ [33]. These coverages require up to 4 hours of incubation in probe. The pulsing method developed by Schumann et al. (which we based our method on) was only able to produce a surface cover of 6.85 x $10^{12}$ molecules per $cm^2$ using a 1 μM probe solution after 15 minutes [34]. We were able to obtain a maximum surface coverge of 1.6x$10^{13}$ molecules per $cm^2$, higher than that obtained via passive incubation as reported by Tarlov et al. and higher than obtained by Schumann using pulsing. Tarlov may have obtained a smaller surface coverage because the DNA strands were longer, leading to more interstrand repulsion and lower DNA density. In addition to a larger surface coverage, we were able to produce that surface coverage in a fraction of the time of the passive method. Furthermore, compared with our past results using the passive method, the pulsing routine increases the reproducibility significantly. According to Figure 28, the passive method, using our standard conditions, resulted in an RSD value of 40% [32]. When using the pulsing method, that value shrunk to around 10% for all but the lowest surface densities (i.e the lowest probe concentration used here, 0.0625 μM). The introduction of the pulsing method allowed for more consistent, reproducible, and rapid preparation of DNA modified electrodes.

Using Figures 26 and 27, a calibration curve was constructed comparing the surface coverage of probe to the MB signal using the pulse assisted procedure. Tagged probe was pulsed at 1 μM, 0.5 μM, 0.125 μM, and 0.0625 μM. After modification of the electrode with tagged probe and MCH, the SWV of the label was acquired. Next, a RuHex assay was acquired on the same electrode. These data points where then used to construct the calibration curve (Figure 29). Using the linear best fit line, MB signal can be directly correlated to surface density without the use of RuHex assay each time (under a given set of experimental conditions).

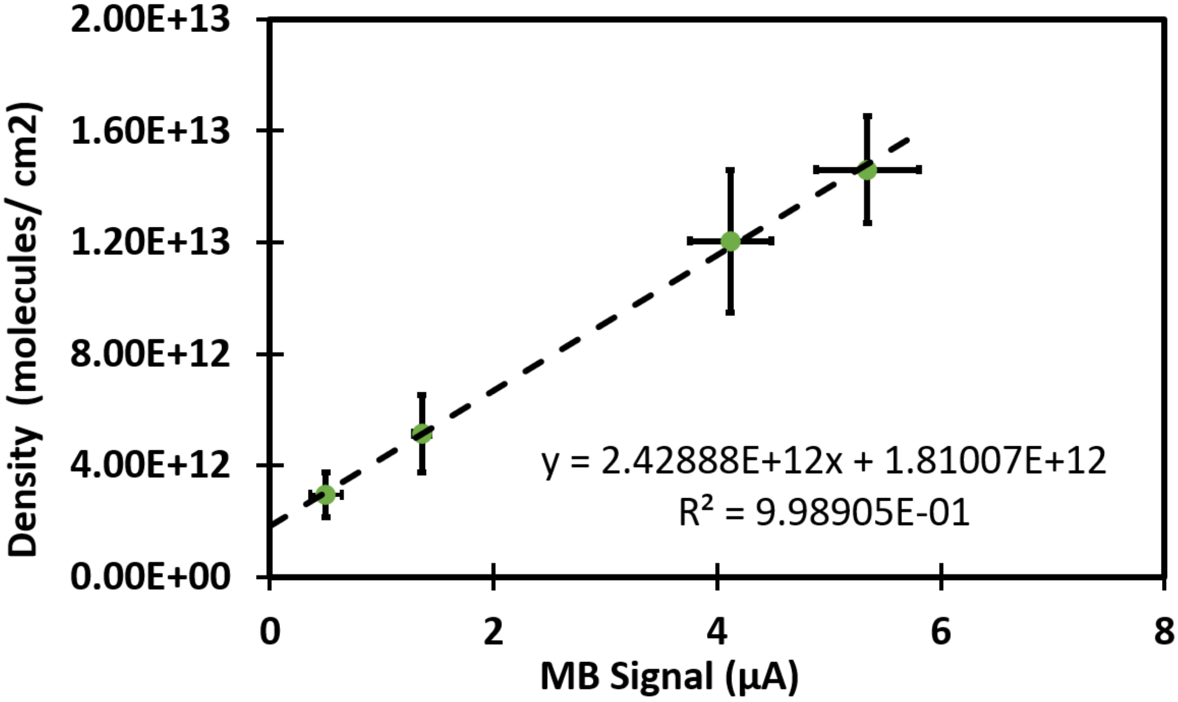

**Figure 29:** Calibration curve showing the density vs SWV Peak Current. A linear relationship can be seen between the two. A larger probe concentration leads to a larger density and MB signal.

Next, we investigated the extent of hybridization as a function of surface coverage. Previously, 100% hybridization was difficult to achieve in dense DNA monolayers [33]. At high DNA densities, both steric and electrostatic effects inhibit complete hybridization. Incomplete hybridization could lead to lower MB peak height for otherwise high probe densities. Four different hybridization times were applied with the hypothesis that increasing time would lead to higher surface densities obtained using the pulsing technique described above. These hybridization times were 40 minutes, 2 hours, and 24 hours and the tagged target was hybridized at four different probe concentrations. After hybridization, the signals were converted to density using the calibration curve from Figure 29. The results are shown in Figure 30, where black dots represent the calibration curve (signal of tagged probe), dark blue represents 40 minutes of hybridization, light blue represents 2 hours of hybridization, and orange represents 24 hours of hybridization. The data suggests that at least 40 minutes was needed for hybridization for all probe densities used here, and 2 hours guaranteed nearly complete hybridization under these conditions. Further experimentation has shown 5 µM target solution can be used to hybridize at room temperature. Tarlov et al used a lower concentration of target and similar hybridization time of 1 µM probe for 1 hour at 35 °C [33].

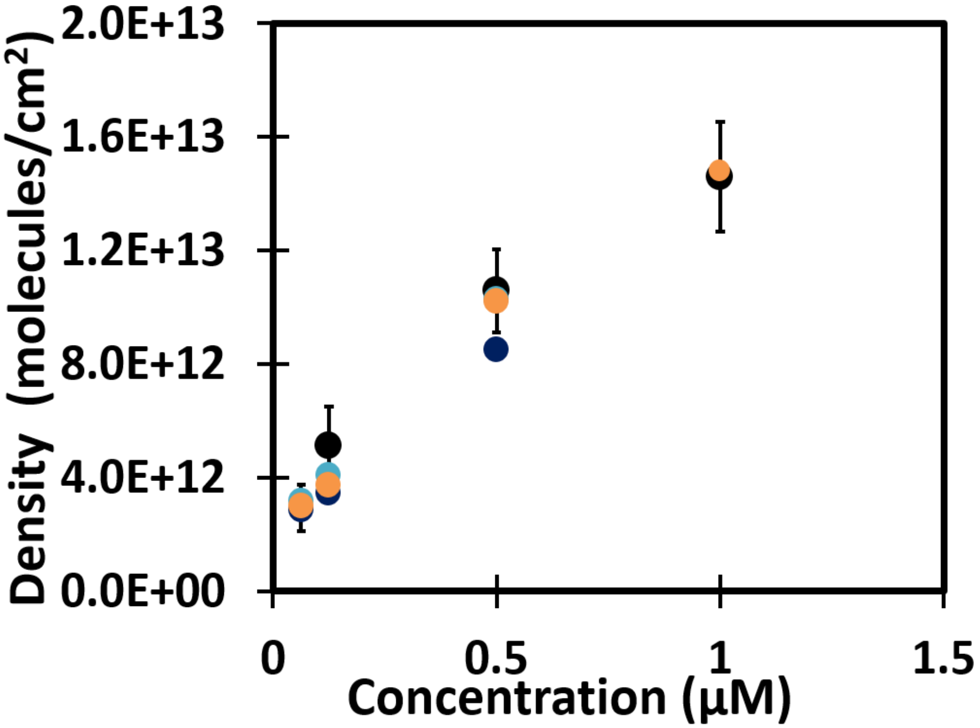

**Figure 30:** The calibration curve (black) was compared to three different hybridization times, 40 minutes (dark blue), 2 hours (light blue), and 24 hours (orange). Within 40 minutes nearly full hybridization occurs.

### *4.5 Electrostatic Denaturation - Effects of Surface Density and Ionic Strength*

In previous electrochemical melting studies, little attention has been paid to the effects of surface density and ionic strength. These two factors are assumed to greatly affect the electrostatic repulsion within the DNA monolayers and therefore affect the stability of the DNA duplexes and the electric fields within the monolayers. It is essential to understand these factors because depending on the electrode conditions, the melting behavior can be different for different experimental conditions, even when duplex stability is otherwise the same (i.e. base pair sequence is the same) which can lead to a bias interpretation.

For the effect of density on electrochemical melting behavior, the pulse-assisted procedure was used to prepare electrodes with four different probe surface densities. These electrodes were hybridized for 1 hr and then electrochemically melted as described in the experimental section. The resulting melting curves were fit to obtain the time constant and melting extent. From the calibration curve, the initial signal was converted to density using the calibration curve. The time constants and melting extents were plotted versus density to see if a correlation was present (Figure 31).

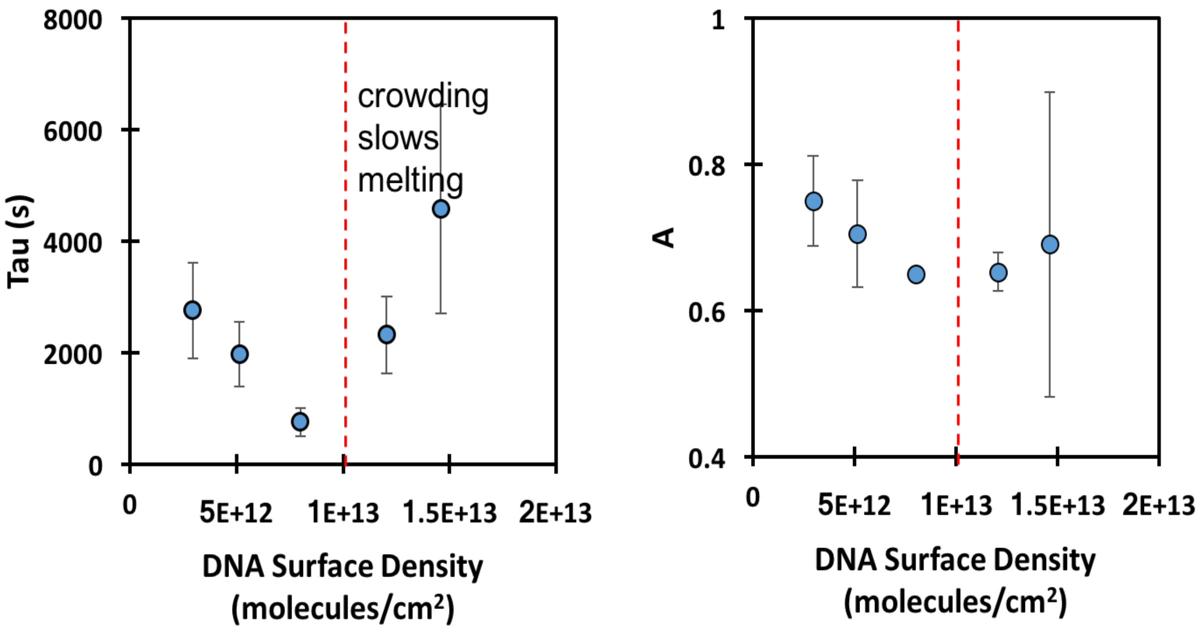

**Figure 31:** DNA surface density is compared to the tau and A values where tau represents the rate of melting and A represents the extent. At a larger surface density, tau increases or the rate of melting decreases. At a smaller value the reverse is true. There does not seem to be a correlation between the extent of melting and surface density

The first conclusion is that when density decreases or increases beyond ~8 x $10^{12}$ molecules per $cm^2$, tau and A both increase. The rise in tau gives some indication that melting occurs more slowly, while the rise in A gives some insight that the extent of melting is greater. The results suggest that at high densities, the steric effects may prevent target from dehybridizing efficiently. This leads to sluggish diffusion of DNA away from the electrode, thus slowing the apparent melting rate. Furthermore, high surface coverage can lead to cross-linking between neighboring strands which will also slow down the melts. Although it’s shown that the kinetics are slowed, the overall extent of melting increases due to the increase of electrostatic repulsion, which overall destabilizes the DNA, shifting equilibrium toward separated target and probe. On the other hand, at low densities, ions from the solution are expected to easily permeate through the DNA monolater to the electrode surface. Thus, allowing for shielding most of the DNA's length from the electric field at the surface. This is expected to not only slow-melting but to again increase the extent, since the proximal end of the DNA is expected to experience even larger electric fields due to the more rapid drop in potential caused by the efficient screening on electrode charge. These factors are balanced at intermediate surface coverages, where melting is faster but to lower extents.

### *4.6 Effects of Salt Concentration on Melting*

For all the experiments discussed so far, melts are carried out in a 10 mM Tris buffer, pH 7 without electrolytes. However, the ionic strength of the solution plays a large role in both stabilizing DNA duplexes and screening of the electrode charge. A higher ionic strength is more effective at shielding the phosphate backbone from the negative electrode charge [36]. This hints that a higher ionic strength should increase the stability of DNA when melting, leading to larger values of time constant and lower melting extent. To explore this, electrodes were prepared and melted using the same routine as above but with different concentrations of NaCl (50, 100, 250, 500 and 1000 mM) added to the buffer. The results can be seen in Figure 32. The change in ionic strength appears to be small except for NaCl concentrations around 500 mM. At an intermediate amount of NaCl, an increase in the time constant and a decrease in melting extent can be seen. More studies are currently underway to better understand both the effect of ionic strength and surface density.

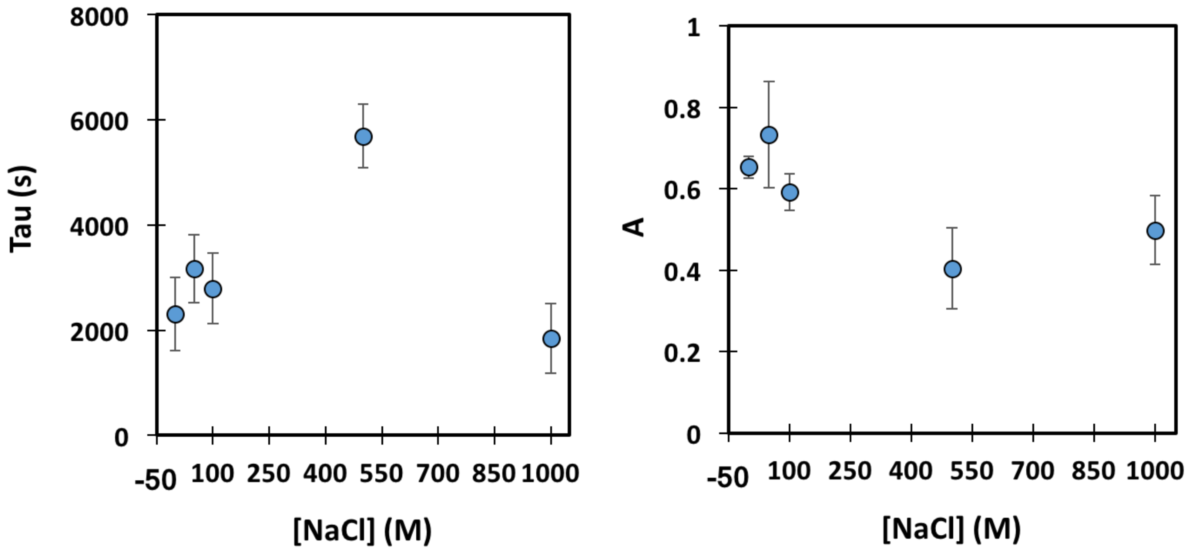

**Figure 32:** E-melting was done at different NaCl concentration and compared to Tau and A. Stabilization of the duplex occurs most readily at the 500 mM mark as indicated by an increased Tau and a decreased A.

Another aspect that was explored regarding salt concentration was initial signal. The initial signals of the electrodes were taken, after the standard probing and hybridization procedure. Next, two of the electrodes were placed in a 50 mM NaCl buffer solution while three electrodes were placed in a 100 mM NaCl buffer solution. The initial signals in the Tris buffer with and without NaCl were then compared. As seen in Figure 33, placing the electrodes in a 50 mM solution decreases initial signal by around 13 % while placing electrodes in a 100 mM solution decreases initial signal by around 20%. This shows that at higher salt concentrations, initial peak current varies, even if prepared under standard conditions (the surface densities do not change). The reason for this is not currently clear but may indicate that the environment of the MB changes depending on the ionic strength. For instance, MB is expected to bind to the major groove of DNA and intercalate. Which of these interactions dominates will depend on the ionic strength. This may account for the change in signal strength. This also means that the calibration curve listed in Figure 29 only applies to 0 mM NaCl melts and not to other salt concentrations. Furthermore, since the concentration of ions in the monolayer may vary as a function of DNA density, and even during progress of the melt itself, SWV peak heights of MB may change due to both removal of target as the melt proceeds and changes in ionic atmosphere in the layer. These factors will be considered more fully in future work.

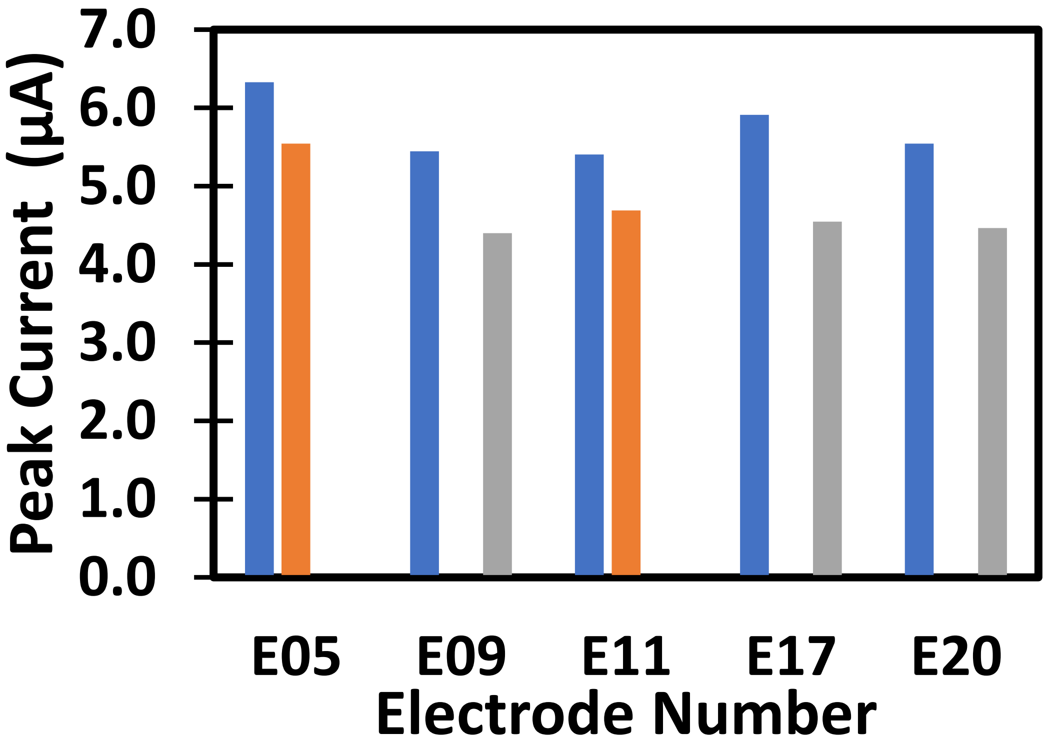

**Figure 33:** 5 electrodes had initial signals taken in 0 mM NaCl (blue). Then they were placed in either 50 mM (orange) or 100 mM (grey) and initial signals where compared. In higher ionic strength solutions, MB signal decreased.

### *4.7 Pulse Melting*

Another goal of this project was to decrease the amount of time needed to run each experiment. Shorter melts will not only decrease analysis time, but also improve the data analysis, as longer melts, with time constants on the order of the experiment time cannot be fit as accurately. To try to increase melting rate, pulse melting was implemented. During a pulse melt, a constant potential is not held during the destabilization phase. Instead, the voltage is pulsed between two different voltages [35]. Like the pulse routine used during adsorption of probe, it is proposed that varying the potential over the course of the destabilization period will lead to a stirring effect, causing an increased ability for melting to occur. The results of pulse melting can be seen in Figure 34. In addition to pulse melting, the removal of the equilibration step was also explored. It is hypothesized that the 10 seconds at -100 mV is positive enough to rehybridize a small fraction of DNA before a SWV can occur. By removing it, DNA melting rate should increase. The traditional melt A (8 minutes at -500 mV followed by 10 s equilibration step at -100 mV), was compared to B (-100 to -500 mV 10 ms each for 8 minutes) and C ( -500 mV 8 minutes no equilibration). In experiment B, a large tau value was obtained. This large tau value was not expected but is most likely due to the pulses being faster than the charging time of the electrical double-layer. If the ions cannot respond to the electrode charge, the screening of the charge (over 1-3 nm) cannot occur, and thus the necessary electric fields do not have time to generate. This hypothesis is currently under investigation. With the removal of the equilibration step (experiment C) tau decreased, as expected. This can be interpreted that the equilibration step prevents dehybridization of the DNA due to having a more positive potential than the destabilization potential (-100 mV vs. -500 mV).

In addition to comparing pulse melting with and without equilibration steps, a new pulsing method called rapid SWV was also compared. It is proposed that multiple SWV scans can promote dehybridization due to having a longer exposure to a negative scanning potential. During rapid SWV, SWV is done every 10 seconds for the course of the experiment. The experiments that were done with rapid SWV are shown in Figure 34 experiment D (-500 mV 10 seconds followed by SWV), and E (-500 mV 10 seconds, -100 mV 10 seconds followed by SWV). This set of data not only compared with and without equilibration steps once more but also looked to see how equilibration steps affected the rapid SWV technique.

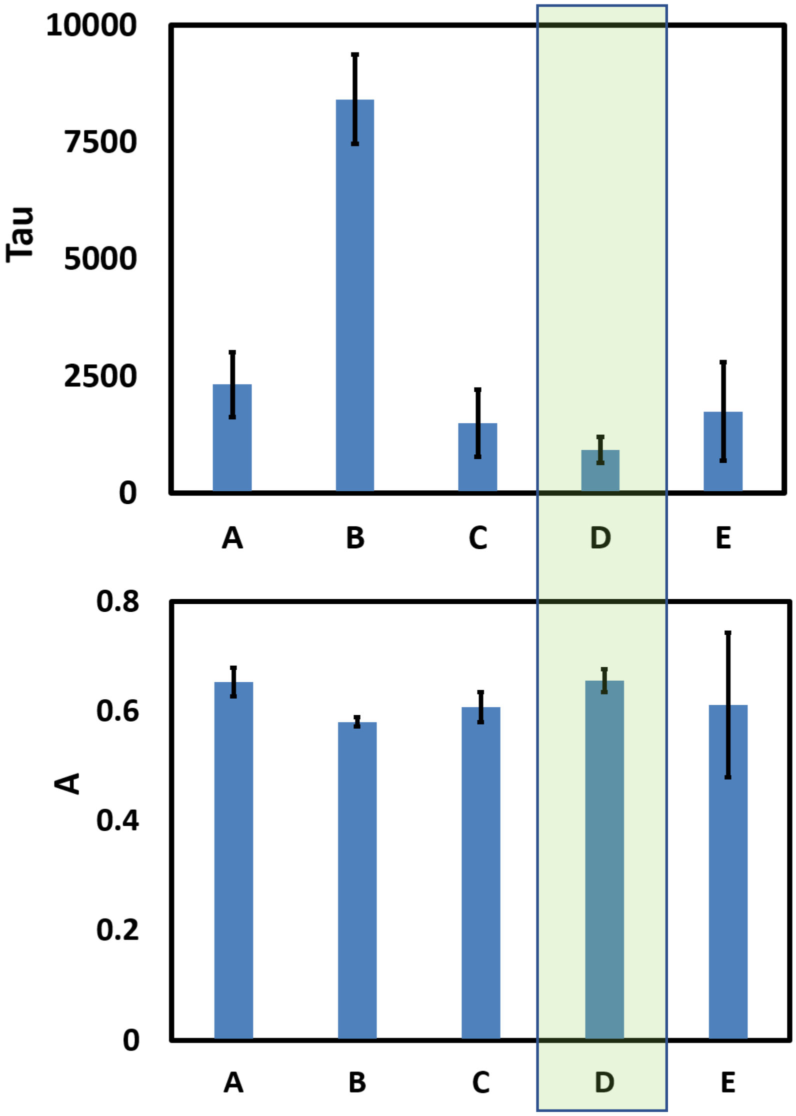

**Figure 34:** 4 different melts where done and compared to the traditional melt (A). (B) -100 to -500 mV, 10 ms each for 8 minutes, (C) -500 mV for 8 minutes, (D) -500 mV 10 seconds followed by SWV, (E) -500 mV 10 seconds, -100 mV 10 seconds followed by SWV. Rapid SWV without the equilibration step (D) is shown to have a faster and more consistent melt.

The results imply that the removal of the equilibration steps leads to a faster melt in the traditional melt and the rapid SWV melt as indicated in Figure 34D. This faster melt can be interpreted as the equilibration step preventing the target from dissociating/diffusion away. Also, the fastest out of the four is the rapid SWV melt without the equilibration step.

## Conclusion

Utilization of a pulse method to attach probe has led to an increase in the reproducibility of the data and better control over surface density has been achieved. A large density of probe leads to a longer melt due to steric interactions and small destiny of probe also leads to longer melt due to increased stability of the duplex. Increasing the salt concentration decreases the rate of melt due to the stability of the duplex with maximum stabilization at 500 mM NaCl. Pulse melting can increase or decrease the rate of melting with rapid SWV melts with no equilibration step causing DNA to melt the fastest. With the optimization of the biosensor complete, drug-DNA interactions can be looked at. Specifically, cisplatin will be added and changes in melting behavior will be observed.

# Chapter 5 Biosensors and Cisplatin

## 5.1 Introduction

Cisplatin, or *cis*-[$PtCl_2(NH_3)_2$], is a common anti-cancer drug used to treat testicular, bladder, ovarian and cervical cancers [37]. It was first discovered in 1965 by Dr. Barnett Rosenberg when he was doing an experiment regarding with *E. coli*. He noticed that when cells divided, they looked identical to how iron shavings look under a magnetic field. Because of this observation, he proposed an experiment on the effects of electric field on cell division. This experiment involved *E. coli* being placed in an ammonium chloride buffer. A current was then applied through "inert" platinum electrodes. It was noticed that as soon as the current was applied to the *E. coli*, the cells stopped dividing. When the current was removed, the *E. coli* began dividing again. At first, Dr. Rosenberg proposed that the electrical current was causing a halt in cellular division. After further studies, it was found that cell division was not being controlled by electrical current but rather by the platinum electrolysis products formed from the platinum electrodes. Out of the many platinum products found, cisplatin was shown to be the compound responsible to inhibit cellular growth. Given the effects of cisplatin, it was proposed by Dr. Rosenberg that this compound could block cell division in tumors. To investigate this hypothesis, two different types of platinum complexes were tested on the tumors in mice. These complexes were the Pt (II) complex, *cis*-[$PtCl_2(NH_3)_2$], and the Pt (IV) complex, *cis*-[$PtCl_4(NH_3)_2$]. In high doses, both complexes were found to be highly toxic to the mice causing kidney failure. [37] In lower doses, the complexes were shown to shrink tumor cells and mice were cancer-free within six months. [37-38]

Cisplatin was first synthesized chemically in 1845 by Michel Peyrone [38]. The early synthesis of cisplatin was slow, unreliable and impure. In 1970, S.C. Dhara developed a new quicker method to synthesize cisplatin. It took advantage of the trans effect to create the correct stereoisomer. The schematic of the synthesis of cisplatin can be seen in Figure 35. The starting material, $K_2\,[PtCl_4]$, is combined with a saturated solution of KI to create $K_2\,[PtI_4]$. Ammonia is then added creating the intermediate triiodo species. Because of the trans effect, the second ammonia attaches trans to the first ammonia ligand creating *cis*-$[PtI_2(NH_3)_2]$. After the addition of $AgNO_3$ and KCl, cisplatin is formed.

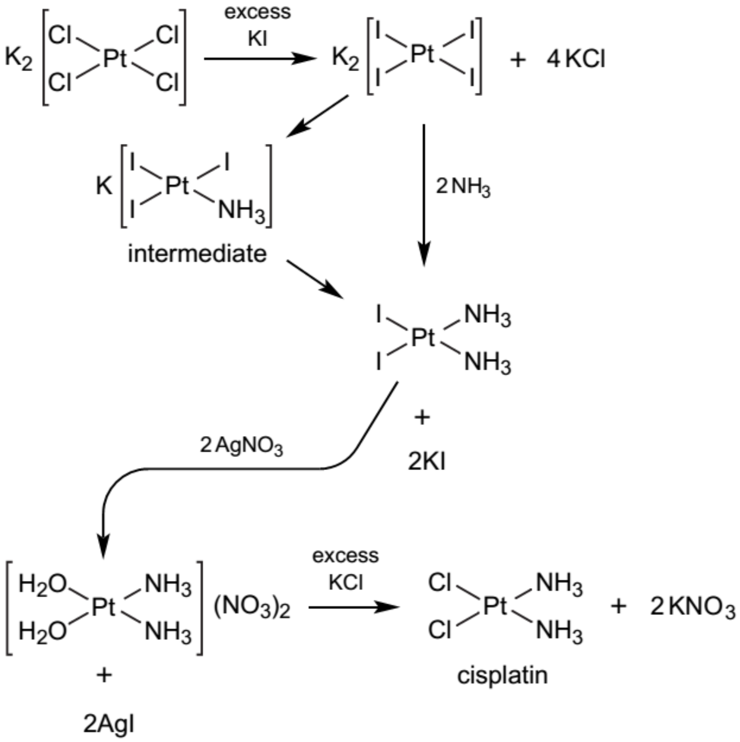

**Figure 35:** The synthesis of cisplatin [38].

In aqueous solution, the two chloride ligands in cisplatin are replaced by aqua ligands, thus activating the compound for binding to DNA [39]:

$$[Pt(NH_3)_2Cl_2] + H_2O \rightarrow [Pt(NH_3)_2Cl(H_2O)]^+ + Cl^- \tag{15}$$

$$[Pt(NH_3)_2Cl(H_2O)]^+ + H_2O \rightarrow [Pt(NH_3)_2(H_2O)_2]^{2+} + Cl^- \qquad (16)$$

The aquated form of cisplatin binds to DNA mainly through the N7 atoms of purine bases [40] with a preference for guanine over adenine [41]. This binding interferes with DNA repair and inhibits DNA replication in the cell. During treatment, cisplatin is administered in the bloodstream. Once it enters the bloodstream, the high chlorine concentrations prevent aquation or the binding of water molecules. Because of this, cisplatin is highly vulnerable to attack by proteins in the blood. It is shown that around 70% of all cisplatin introduced is bound to proteins. The binding causes deactivation of the cisplatin and is part of the reason why severe side effects occur [38]. Nonbonded cisplatin then enters the tumor cell through transporting proteins. Due to the lower concentration of chloride in the cell membrane, aquation occurs. 98% of cisplatin binding occurs with monoaquated cisplatin [38]. The monoaquated cisplatin then preferably binds to the N7 guanine. The second chlorine is then aquated allowing binding to a G, C or A residue. Around 65% of binding occurs between GG base pairs [38]. Once cisplatin binds, it distorts the DNA structure and DNA binding proteins do one of two things: they either signal for cell death or for DNA repair. Since bonded cisplatin has a chance to not cause cell death due to DNA

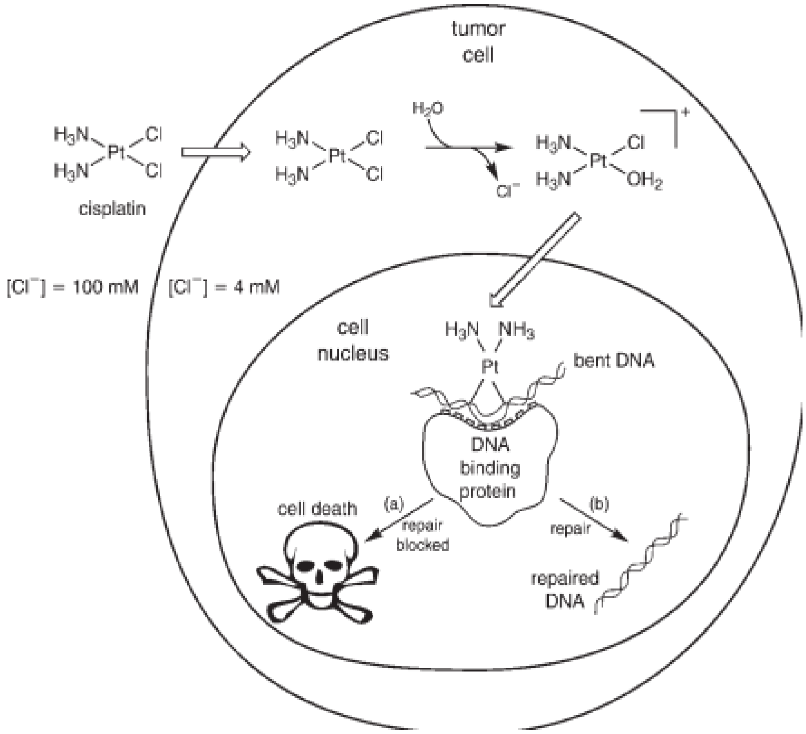

**Figure 36:** A simplified diagram showing the interactions of cisplatin. The binding of cisplatin can lead to cell death or DNA repair [38]

repair, it can be difficult at times to determine if cisplatin is affecting the cell. A simplified schematic of the biochemical pathway of cisplatin can be seen in Figure 36.

Cisplatin can partake in interstrand and intrastrand binding to DNA, with intrastrand binding between adjacent guanine bases being the most common both *in vitro* and *in vivo* [42]. The double-helix of the resulting cisplatin-DNA adduct is distorted, leading to a perturbation of the base stacking, a partial shift from the B-form to the A-form, and a decrease in melting temperature by approximately 9 ºC [43]. This reduction in thermal stability is enthalpic in origin. Other binding possibilities include intrastrand cross-linking between guanines separated by one base, intrastrand cross-linking between an adjacent guanine and adenine, and interstrand cross-links between guanines and adenines. Interstrand crosslinks have been shown to increase thermal stability by up to 12 ºC [44,47]. The overall effect on stability has a strong dependence on the ionic strength [45].

In order to study the effects of cisplatin and other organometallics on DNA, biosensors have been developed using electrochemical methods. Due to cisplatin's affinity toward guanine, voltammetry can be used to study the oxidation peak of guanine during cisplatin binding. For instance, Bagi et al. created a printed electrode consisting of silver working electrode and graphite working and counter electrodes [46]. DNA was then physisorbed on the working electrode at +0.5 V for 5 minutes. SWV was then implemented on the printed electrode from 0.2 V to 1.4 V to measure the oxidation of guanine residue on the electrode surface. Because cisplatin interacts directly with guanine, a decrease in oxidation current of guanine was observed [47]. In this range, an adenine peak was also detected but was not used due to cisplatin's higher affinity for guanine. An example of the peak heights for adenine and guanine can be seen in Figure 37a [46].

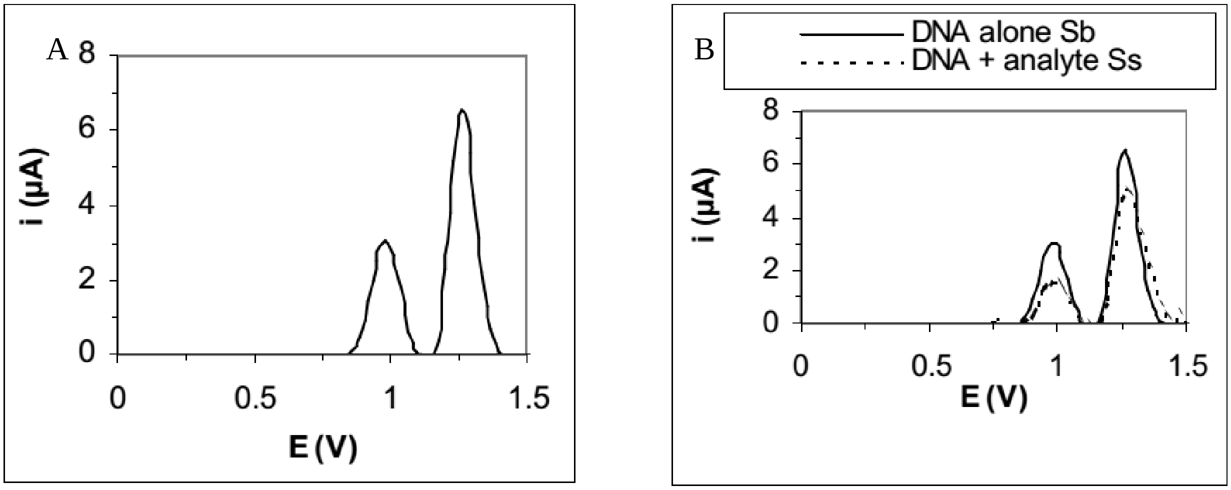

**Figure 37:** The oxidation peak of adenine, left peak, and guanine, right peak, are detected through SWV. (b) When a denaturing analyte is added, both the adenine and guanine peak have a decrease in current. [46].

Cisplatin and other platinum-based drugs were then introduced into the solution. To begin, the electrode was placed in a 0.1 mM cisplatin solution with 5 mM NaCl and 100 mM NaCl. A reduction of the peak heights was observed upon introduction of cisplatin, as shown in Figures 37b and 38. In particular, Figure 38, shows the time and salt dependence of the effect, with a larger decrease occurring at lower NaCl concentration after 3 minutes of equilibration time.

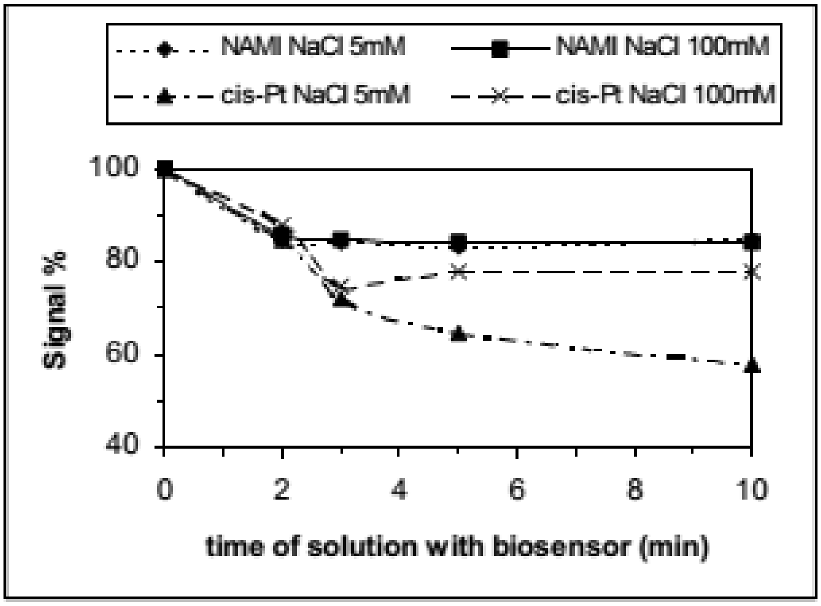

**Figure 38:** The effect of cisplatin binding was determined through a decrease in the oxidation of guanine. A low salt cisplatin solution causes the highest amount of destabilization to occur resulting in a lower percent signal. [46].

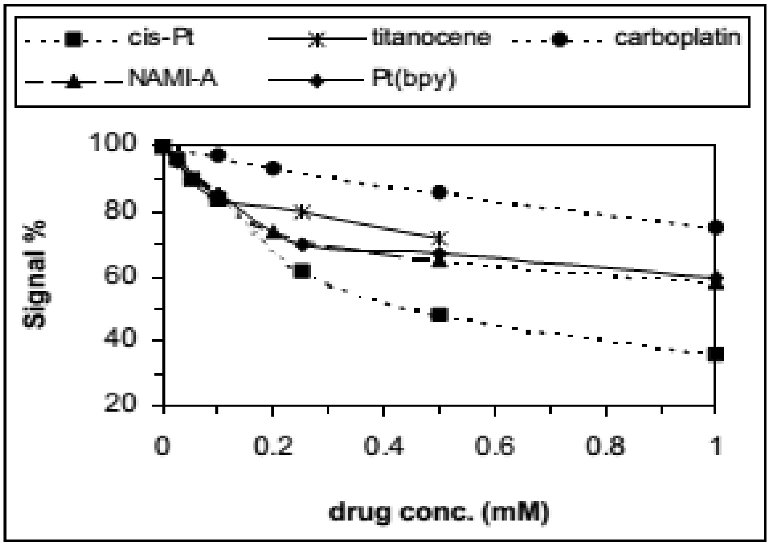

**Figure 39:** Comparison of guanine signal change with drug concentration of 5 different drugs. Cisplatin is shown to have the largest effect on the oxidation of guanine. [46]

In addition to time of exposure, concentration of cisplatin was also explored. Time and salt concentration where kept consistent at 2 min and 5 mM NaCl respectively. The results are shown in Figure 39. Cisplatin is seen as having the largest effect on the oxidation of guanine compared to other platinum drugs shown in the figure with the effect increasing with concentration.

Electrochemical detection of cisplatin-DNA adducts were also examined by Fojta et al. [47]. In this work, DNA was incubated it with cisplatin overnight. Next, the mixture was mixed with magnetic beads that only bonded with the DNA if cisplatin was present. The beads were then washed allowing separation of the beads and the cisplatin bounded DNA. DNA stands were then analyzed using SWV. A diagram of this procedure can be seen in Figure 40.

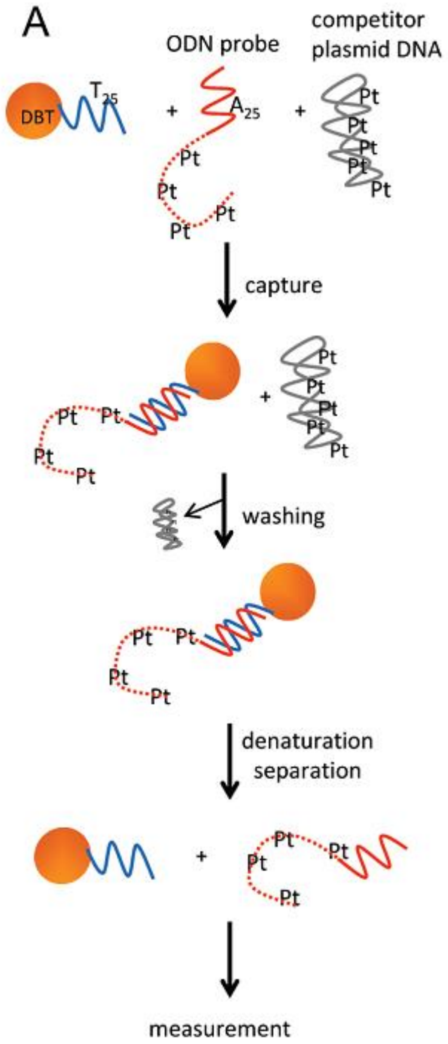

**Figure 40:** A mixture of probe and DNA plasmid was mixed with magnetic beads (DBT). This bead captured the probe and left the plasmid behind allowing to isolate DNA cisplatin interactions versus plasmid DNA cisplatin interactions [47].

To test the detection of cisplatin, both a hanging mercury drop electrode (HMDE) and graphite electrode were used. The DNA was exposed to four different *rb* values of cisplatin where rb is the number of platinum atoms bound per DNA nucleotide. A SWV was then taken and peak current was observed. The results can be seen in Figure 41 [47].

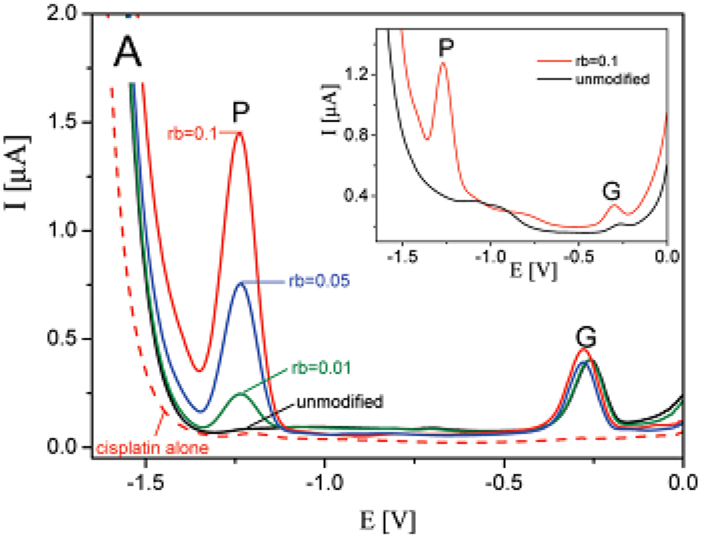

**Figure 41:** A SWV was taken of the DNA sample. Four different solutions of DNA were used. Each one contained a different modification level of rb. The G peak (graphite electrode) saw little change when different rb values were done. The P peak (HDME) shows a drastic change. More platinum binding (larger rb) gave a larger current. [47]

In Figure 41 the SWV peaks are shown using both a graphite electrode and HDME. The graphite electrode is unable to distinguish the different modification levels of the DNA. It is, however, able to discriminate between cisplatin bonded to the DNA and free-floating cisplatin. The HDME is not only able to distinguish free-floating cisplatin from bonded cisplatin, but also able to clearly show the modification levels of the DNA. The larger the *rb* value, the larger the current. These results demonstrate the power of electrochemical methods for measurement of cisplatin-DNA binding.

More recently, an electrochemical quartz crystal microbalance was used to study the effect of cisplatin binding in DNA self-assembled monolayers (SAMs) [48]. In this study, the effect of cisplatin binding on the viscoelasticity of the SAMs was evaluated. The authors found that extensive cross-linking of the DNA led to increased rigidity and a decrease in the frequency response.

In this work, we utilized self-assembled monolayers (SAMs) of DNA on gold electrodes, to analyze DNA-cisplatin interactions. SAMs of double-stranded DNA (dsDNA) have been used to study DNA hybridization, thermal melting, and DNA-small molecule interactions. In all of these applications, the DNA monolayers are responsive to high electric fields at the electrode-electrolyte interface [49]. This behavior is typically attributed to the negatively charged sugar-phosphate backbone at neutral pH. Sufficiently negative electrode charge can cause dsDNA to denature, releasing the “target” strand from the electrode in a process termed *electrochemical melting* [50-52]. The potential and rate at which electrochemical melting occurs are dependent on the length, sequence, complementarity, and overall stability of the duplex. Thus, electrochemical melting analysis can provide biophysical insights into the effects of electric fields on DNA structure and stability, which may further our understanding of DNA behavior in the cellular environment [53-54]. Furthermore, the possibility of discriminating DNA-containing samples based on the presence of particular sequences or mutations opens the way towards diagnostic applications of electrochemical melting analysis. For instance, recently our lab has demonstrated a purely electrochemical approach that minimizes thiol desorption and allows discrimination based on the presence of a single mismatched base pair [32]. Despite these possibilities, the mechanism of electrochemical melting is not fully understood [54-56].

In this work, we report on the electrochemical melting of surface-bound DNA in the presence of cisplatin. We find a striking difference in the effect of electrochemical melting depending on the method of monolayer preparation. This difference is rationalized in terms of the DNA surface coverage and heterogeneity. In particular, we postulate that the local interstrand distances and ionic environment determine the mode of cross-linking by cisplatin and thus the electrochemical melting behavior. Surface coverage has previously been shown to play an important role in hybridization [57-58], thermal melting [59] at surfaces, and on the electrical modulation of DNA orientation [60-61]. Furthermore, the electrostatic environment and the distribution of ions within the electrical double-layer are expected to depend on surface coverage [61-62]. The effects of DNA surface coverage and the heterogeneity of the surface coverage on electrochemical melting have not yet been reported [63]. Our results here suggest (1) electrochemical melting analysis can provide details about the mode of cisplatin binding in crowded DNA environments, and (2) may lead to a possible electrochemical procedure for indirectly assessing the local interstrand distances resulting from different monolayer preparations procedures.

## *5.2 Methods and Materials*

*5.2.1 Chemicals and equipment*. All chemicals were purchased from Sigma-Aldrich and used as received. The modified oligonucleotides used in this work were purified by dual high performance liquid chromatography (LGC Biosearch Technologies, Petaluma, CA). Both probe and target sequences contain 18 base pairs and are fully complementary with each other. The probe oligonucleotide is labeled with a thiol group via a 6-carbon linker on the 5' end (5'HS-C6-TTG ATC GGC GTT TTA TTC 3'). The target oligonucleotide is labeled with a methylene blue (MB) moiety on the 3' end (3' MB-AAC TAG CCG CAA AAT AAG 5'). Five buffers were used in this work. Solutions of mercaptohexanol (MCH) and thiolated probe DNA were prepared in 10 mM phosphate buffer containing 2.7 mM KCl and 1.14 M NaCl (pH 7.4). Hybridization of surface-bound probe and target was carried out in 10 mM Tris containing 1 M NaCl and 1 mM EDTA (pH 7.2). Electrochemical melting was performed in 10 mM Tris buffer (pH 7.2).

Electrodes were rinsed in 5 mM Tris buffer containing 10 mM NaCl (pH 7.2). All solutions were prepared using deionized water.

All electrochemical experiments were carried out using polycrystalline gold disk working electrodes (geometric surface area 0.0314 cm$^2$ and roughness factor ca. 1.4), Ag/AgCl (1 M KCl) reference electrode, and platinum wire counter electrode (CH instruments, Austin, TX). Electrochemical melting was carried out using a VersaStat 4 potentiostat and VersaStudio software (Ametek Scientific Instruments, Berwyn, PA) at a temperature of 30 °C. Electrochemical polishing was carried out on either a VersaStat 4 or a WaveNow (Pine Research, Durham, NC) potentiostat.

*5.2.2 Electrode cleaning.* The gold working electrodes were cleaned in a 3-step process consisting of a mechanical polish followed by two electrochemical polishing steps. First the electrodes were mechanically polished with 0.3-micron alumina slurry for 3 minutes in a figure-eight pattern. The electrodes were subsequently sonicated in methanol for 1 minute, rinsed with deionized water, and sonicated again in deionized water for 1 minute. These sonication steps were repeated a total of 3 times. Next, the electrodes were cycled in 0.5 M $H_2SO_4$ with 10 mM KCl solution from 0.24 V to 1.54 V at 0.1 V/s for 60 cycles. The electrodes were rinsed with deionized water and then cycled in 0.5 M $H_2SO_4$ using the same parameters.

*5.2.3 Preparation of DNA-modified gold electrodes.* DNA-modified electrodes were prepared using one of three different procedures; (1) pulse-assisted backfill, (2) passive insertion, or (3) pulse-assisted co-deposition. Details of these methods are presented below. In all cases, prior to probe adsorption, tris(2-carboxyethyl)phosphine-HCl was used to reduce the disulfide bonds of the as-delivered probe. After probe and mercoptohexanol adsorption, the electrodes were incubated in 5 μM target solution for 1-2 hours to allow hybridization. For experiments with cisplatin, 10 µL of 3 mM cisplatin solution (made 24 hours previously) was added to 60 µL of 5 µM DNA target and the electrode was immediately incubated in this solution for 1-2 hours.

*5.2.4 Pulse-assisted backfill method* The probe solution was diluted to 0.5 µM and the gold working electrode was pulsed from 0.5 to -0.2 V at room temperature at 10 ms intervals for 15 minutes. Electrodes were then rinsed for one minute, dried, and incubated in 9 mM 1-mercaptohexanol (MCH) in PBS buffer overnight at 4 $^{o}$C.

*5.2.5 Insertion method.* Gold electrodes were placed in 9 mM MCH for 1 hour. The electrodes were then rinsed for one minute and then placed in 10 µM probe DNA overnight. Finally, the electrodes were placed back in 9 mM MCH overnight.

*5.2.6. Pulse-assisted co-deposition method.* The probe solution was diluted to 0.5 µM and mixed with 9 µM MCH in PBS Buffer. This mixture was pulsed onto the freshly cleaned electrodes using the same pulse routine employed in the pulse-assisted backfill method.

*5.2.7 Electrochemical melting.* The electrochemical melting routine [32] consisted of a programmed sequence of potential pulses, each at -500 mV with a duration of 8 min. Between each pulse, square wave voltammograms were acquired to monitor the amount of MB-tagged target DNA remaining on the electrode surface. After each pulse, but before the acquisition of the voltammogram, the electrode was equilibrated at −100 mV for 10 s. The equilibration step was previously found to result in better quality voltammograms. The SWV parameters were as follows: initial potential = −100 mV, final potential = −450 mV, amplitude = 25 mV, frequency = 167 Hz (unless otherwise noted), and increment = 6 mV. All data in this work was performed in triplicate. The baseline subtracted SWV peak currents were normalized to the initial (pre-melt) peak current and plotted versus time to obtain melting curves. Fast scan cyclic voltammograms

(4 V/s) were obtained before each melting routine in order to assess the DNA surface coverage via integration of the methylene blue reduction peak.

## Results and Discussion

### *5.3 Comparison of Monolayer Preparation*

Self-assembled mixed monolayers of thiolated DNA and alkylthiol (typically mercaptohexanol) are routinely used for development of DNA sensors, molecular electronics, DNA chips, and other applications. Various procedures have been utilized to prepare these mixed monolayers. Three methods were compared in this work: pulse-assisted probe deposition with passive MCH backfilling (referred to as the backfill method from here on), passive MCH adsorption followed by passive insertion of probe (referred to as the insertion method), and pulse-assisted co-deposition of MCH and probe simultaneously (referred to as the co-deposition method).

The resulting distribution of DNA on the electrode surface is expected to affect the conformation of the duplexes [64] the extent of interstrand interactions [65], the steric and electrostatic barriers to hybridization [66], the melting temperature [67-68], and the responsiveness to electric fields [69]. The heterogeneity and overall surface coverage can be controlled by choice of deposition method [70]. While measurements of surface coverage are possible using electrochemical approaches [33,71], as well as radiolabeling and spectroscopic methods [72], these results are averaged over the entire surface, and thus do not provide insight into possible heterogeneity in the surface coverage and the resulting interstrand distances. Recently, there have been reports that mixed monolayers of DNA and MCH are not as homogeneous as previously thought [73]. These studies rely on microscopies techniques utilizing

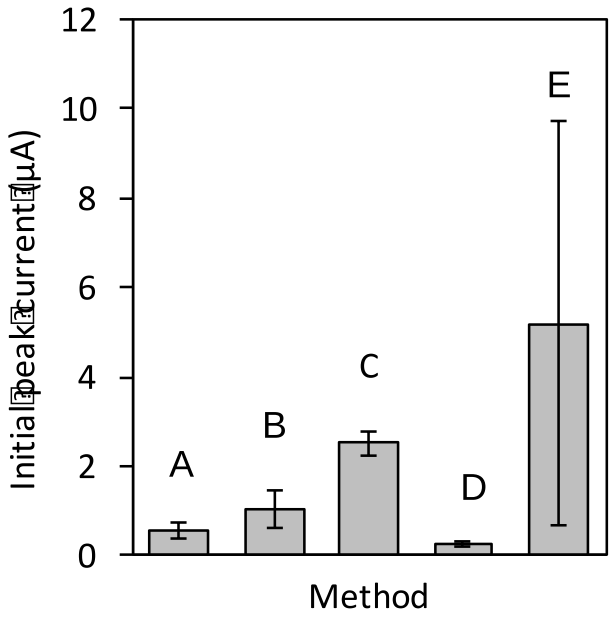

**Figure 42:** Comparison of the initial peak currents for various electrode modification methods: Pulse-assisted probe immobilization followed by MCH backfill for probe concentration of (A) 0.0625 µM, (B) 0.125 µM and (C) 0.5 µM, respectively; (D) insertion method; (E) pulse-assisted co-deposition. A-E lettering is used similarly throughout the text.

fluorescence quenching and other techniques which are often necessary for experimentally accessing surface properties on the nanoscopic scale. Here we utilize an electrochemical approach involving cisplatin to identify heterogeneity in DNA SAMs. In turn, these results allow us to optimize our approach for the study of cisplatin-DNA interactions in DNA monolayers.

Tarlov et al. developed the commonly used backfill method for DNA monolayer preparation, which consists of passive immobilization of thiolated ssDNA followed by "backfilling" with the MCH layer [72]. The adsorption of MCH was shown to remove some non-specifically absorbed DNA from the surface, prevent further non-specific adsorption, and to orient the tethered DNA in an upright position [73-74]. Further improvements in reproducibility and reduction in deposition time can be achieved using pulse-assisted probe mobilization [34] followed by backfilling with MCH. Combining pulse-assisted probe adsorption with the backfill approach, we have obtained readily controllable and reproducible surface coverages, as shown by the initial peak currents in Figure 42. The surface densities are readily varied by controlling the concentration of probe in the deposition solution from 0.0625 µM, 0.125 µM, and 0.5 µM (A, B, and C in Figure 42, respectively).

More recent results indicate that MCH does not completely remove strongly absorbed DNA [75,70], resulting in heterogeneous surfaces containing DNA aggregates [76]. The homogeneity can be improved using the insertion method, which involves reversing the order of adsorption, i.e. adsorbing MCH first followed by DNA [70,77-78]. Here we apply this approach using passive adsorption (i.e. no pulsing) of both MCH (9 mM, 1 hr) and DNA (10 mM, overnight). As seen in Figure 42(D), the insertion method results in relatively low but reproducible surface coverages under the conditions used here. Attempts to increase the surface coverages by decreasing the MCH incubation time only resulted in lower reproducibility (results not shown).

Finally, co-deposition of MCH and probe has been proposed as another method for improving reproducibility and preventing DNA aggregation [79-80]. Here, we combined co-deposition with the pulse-assisted process used above. The electrode was pulsed (using the parameters given in the experimental section) in a solution of 0.5 µM probe and 9 µM MCH. The co-deposition method allowed the largest surface densities but with the lowest reproducibility, as seen in Figure 42 (E). At higher ratios of DNA to MCH, reproducibility was compromised whereas lower ratios of DNA to MCH resulted in very low surface coverages (data not shown).

### *5.4 Electrochemical Melting*

As we have previously demonstrated [32], application of -500 mV (versus Ag/AgCl 1 M KCl) results in denaturation of dsDNA adsorbed to gold electrodes. Covalent modification of the target strand with methylene blue allows electrochemical monitoring of the melting using square wave voltammetry. Figure 43 shows a series of voltammograms taken at 8-minute intervals between application of -500 mV for the 18-bp duplex used in this work. At -500 mV, the potential is negative enough to induce melting, but reduction of the thiol bonds is minimized, therefore the decrease in signal is attributed primarily to electrochemical melting [32]. The lack of significant desorption is also reflected in the constant baseline throughout the duration of the melt.

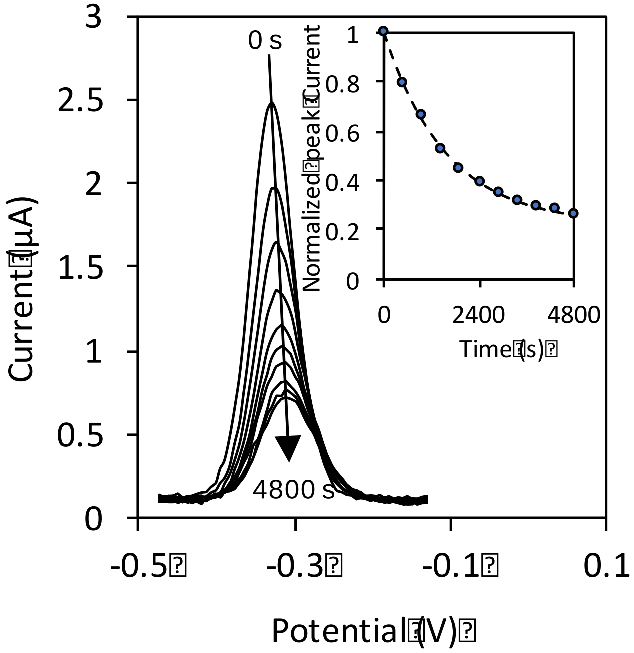

**Figure 43:** Example of square-wave voltammograms during a melt. The inset shows the resulting melting curve with the best-fit curve given by the dashed line. The DNA-modified electrode was prepared using pulse-assisted probe adsorption from 0.5 µM probe followed by passive adsorption of MCH overnight. The melt was carried at 30 °C and -500 mV vs. Ag/AgCl (1 M KCl).

Melting curves were constructed from the voltammograms by plotting the baseline-subtracted peak heights versus time, as shown in the inset in Figure 43. The dashed line shows the best fit equation:

$$i_p = Ae^{-t/\tau} + (1 - A) \tag{17}$$

Where *tau* ($\tau$) is the time constant and $A$ is interpreted as the extent of melting. Tau has previously been shown to depend on the stability of the dsDNA, and in particular provides information about the kinetics of melting and/or the rate of diffusion of released target away from the electrode. The extent of melting depends on the ratio of bound and dissociated target at equilibrium. Since target is not initially present in the buffer and remains essentially zero during the melt due to the large volume used (ca. 5 mL), the extent of melting would presumably be 1, indicating complete melting of all duplexes. In our work, and other's [52,81-82], melting does not proceed to 100%. One possibility is that the dissociated target strands diffuse slowly away from the surface due to low diffusion coefficient (1.4 x $10^{-7}$ $cm^2/s$) [83], allowing a quasi-equilibrium at the electrode-electrolyte interface (no stirring is used here). Though this quasi-equilibrium may contribute to the melting behavior, melting experiments measured over long times show very little drift in the limiting peak current, as would be expected if the slow diffusion were the main reason for this behavior.

We postulate that the extent of melting is both chemical and electrostatic in nature; that the DNA melts *until* counterions from solution can sufficiently screen the negative charge on the electrode. Thus, electrochemical melting is expected to depend on a balance of duplex stability and electrochemical double-layer effects. A similar mechanism has been proposed for hybridization at charged surfaces, i.e. hybridization proceeds until counterions can no longer sufficiently screen the electrode charge [84]. Of course, such a mechanism is complicated by the fact that the DNA itself contributes to the double-layer charge through its phosphate backbone and condensed counterions. Another possible factor related to the double-layer effect involves the shift in the potential of zero charge (*pzc*). As the DNA melts, the *pzc* is expected to shift negative, thus decreasing the electrode charge at constant applied potential [49,85]. While more work is necessary to fully understand factors affecting electrochemical melting, a complex interplay of chemical and electrostatic effects is anticipated, including the ionic strength of the buffer, the density of the DNA monolayer, and the stability of the DNA duplexes, among others.

### *5.5 Effect of Monolayer Preparation on Melting*

While the role of surface coverage on the hybridization and electric-field responsiveness of DNA monolayers has been investigated [59], the effect of surface coverage on electrochemical melting has not previously been reported. Interstrand distance and overall surface coverage are expected to affect the degree of interactions between neighboring strands [65], the negative charge density of the polyelectrolyte layer, and control the distribution of ions across the monolayer-solution interface [61]. Surface coverages obtained through most techniques are surface-averaged and do not reflect the true uniformity of the DNA monolayer. Heterogeneity and aggregation of DNA on the surface can result in shorter probe-probe distances than anticipated from the average surface coverages alone. These factors are expected to affect the electrochemical melting of DNA SAMs. Therefore, we first investigated the melting behavior of DNA SAMs obtained via the three different procedures introduced above, i.e. backfill, insertion, and co-deposition

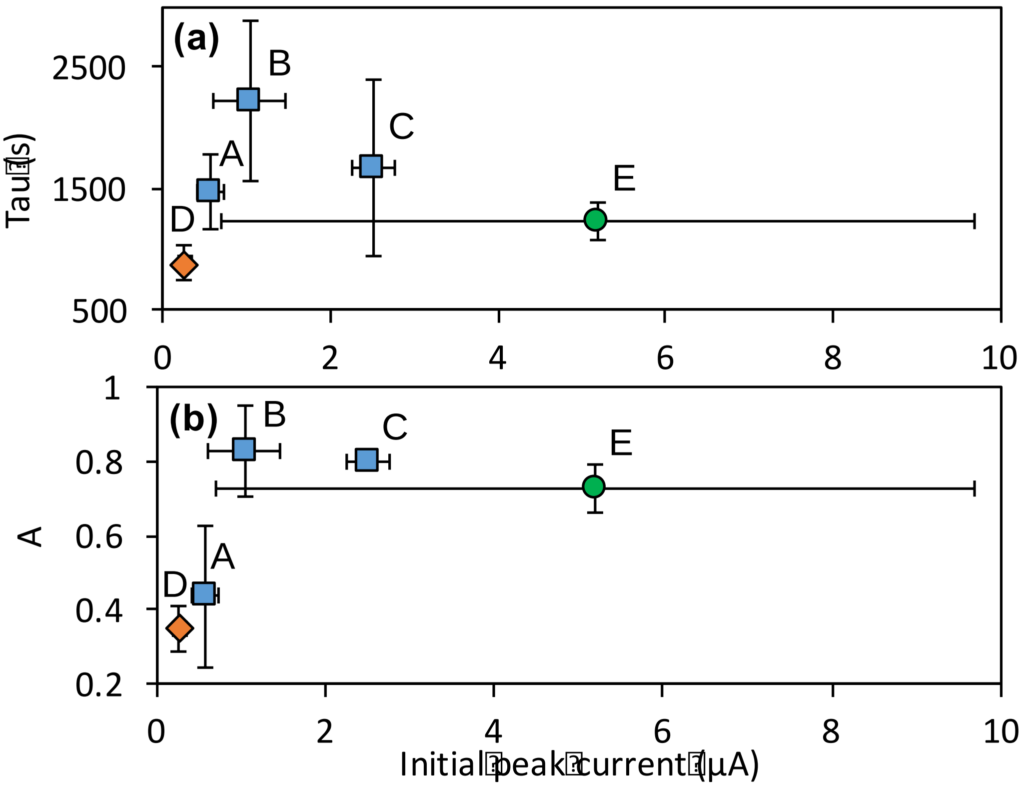

**Figure 44:** Plots of (a) *tau* versus initial signal and (b) *A* versus initial signal for electrochemical melting of dsDNA: (A-C, blue squares) backfill method for probe concentrations of 0.0625 µM, 0.125 µM, and 0.5 µM, respectively; (D, orange diamond) insertion method; and (E, green circle) co-deposition method. Error bars are standard deviations from triplicate measurements.

Given the high degree of control over surface coverages afforded by the backfill method (see Figure 42), it is expected that clear trends would be obvious in the melting parameters *tau* and *A*. As can be seen in Figure 44 (data points A-C), tau values obtained for these films are larger than for the other two methods, indicating slower melting. Methods B and C also result in larger extents of melting than the other methods. Considering that these films are expected to be heterogeneous, and therefore have shorter interstrand distances than anticipated, the larger extent of melting indicates a greater degree of interstrand repulsion and lower overall stability. For the lowest probe concentration (0.0625 µM), the extent of melting is low indicating that in these films the interstrand distances are shorter, presumably due to the lower surface coverage, thus less interstrand repulsion. The larger *tau* values resulting from the backfill method suggests that steric effects may be inhibiting the unzipping and/or diffusion of the DNA into bulk solution. These effects are alleviated as the DNA continues to melt, easing the steric constraints, and eventually allowing the large extents of melting observed. There does not appear to be a linear relationship between surface coverage and *tau* or *A*, instead the *tau* and *A* values reach a maximum at intermediate coverages, i.e. 0.125 μM probe.

The insertion method produced the lowest surface coverages and the resulting films have the lowest values of *tau* and *A* (see Figure 44, data point D). The higher rate of melting suggests that these films contain DNA duplexes that are well separated from each other, allowing faster melting and diffusion away from the surface. The low extent of melting indicates that counter ions readily penetrate the monolayer, allowing sufficient charge screening as melting proceeds to inhibit further melting. Finally, while the co-deposition model provided the least control over surface coverage, these monolayers melted similarly regardless of the initial peak current (as shown by the low standard deviations in Figure 44, data point E). *Tau* is found to be intermediate between the insertion and backfill methods, and *A* is found to be similar to values found for the backfill method. In other words, these films melt fast and to a large extent. Due to the higher uniformity expected in these films, interstrand distances are expected to be larger than for the backfill method but lower than for the insertion method. Thus, the steric factors that slowed melting of backfilled monolayer are not expected to play as large a role here.

### *5.6 Electrochemical Melting of cisplatin-DNA*

Binding of cisplatin to DNA introduces conformational changes in the DNA helix, e.g. a shift from the B-form towards the A-form, and a resulting decrease in thermal stability and lowering of the melting temperature. These effects are expected to alter the behavior of the DNA monolayer during electrochemical melting. There are few reports of electrochemical melting in the presence of DNA-binding drugs. Bartlett et al. studied the electrochemical melting of DNA bound to the anticancer drug mitoxantrone. Upon intercalation, the melting potential shifted negative by 120 mV due to stabilization [86]. There are also reports on the thermal melting of surface-bound DNA measured using electrochemical detection. For instance, Robinson et al. reported on the thermal melting of DNA in the presence of the intercalator proflavine and the minor groove binder diminazene aceturate using a microscale platform with integrated microheater [87]. Here, we use a purely electrochemical approach, at constant temperature, to probe the stability of DNA in the presence of cisplatin, which is known to cross-link DNA strands.

Representative melting curves of DNA with and without cisplatin are shown in Figure 47. Close inspection of the melting curves shows that the cisplatin affects films prepared by the backfill method (here shown only for 0.5 µM probe, Figure 45a) in a qualitatively different way compared to the insertion (Fig. 45b) and co-deposition methods (Fig. 45c). The time constant increases upon introduction of cisplatin for (a) but slightly decreases for insertion (b) and co-deposition (c). On the other hand, the extent of melting decreases significantly for insertion (b) and co-deposition (c), but slightly increases for backfill (a). In all three cases, the presence of cisplatin is readily detected.

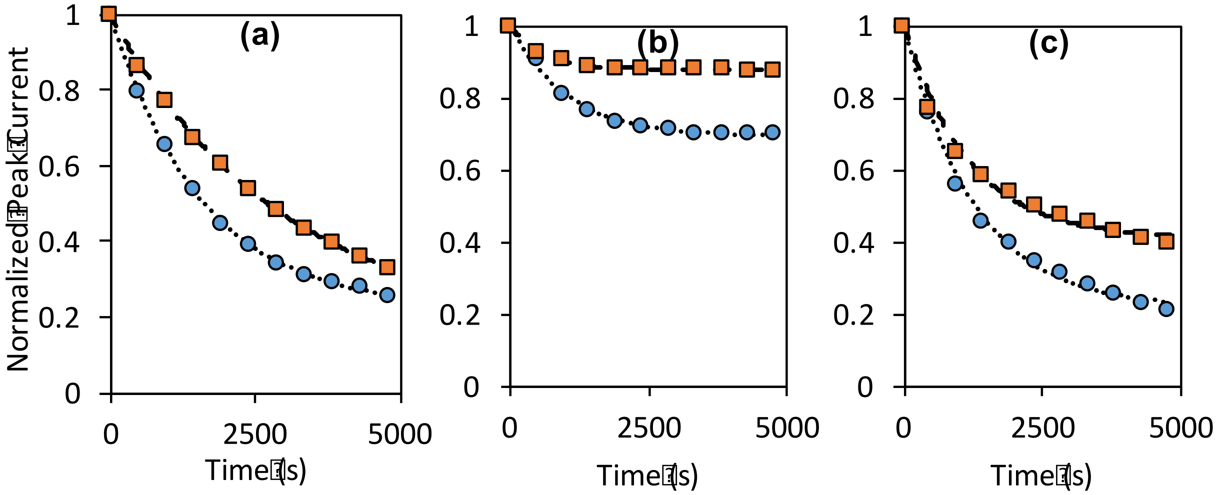

**Figure 45:** Melting curves and exponential fits of dsDNA with cisplatin (data: orange squares; fit: dashed line) and without cisplatin (data: blue circles; fit: dotted line) for the three preparation methods: (a) backfill method with 0.5 µM probe DNA, (b) insertion method, and (c) co-deposition method.

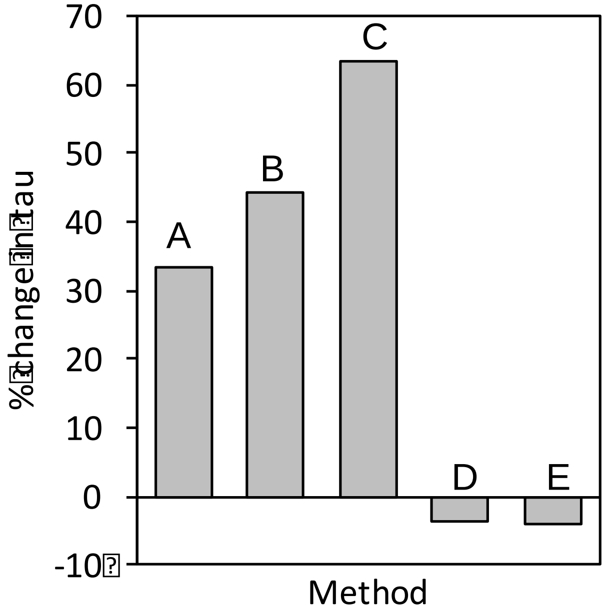

**Figure 46:** Comparison of the % change in tau upon binding of cisplatin for various electrode modification methods: (A), (B), (C) Pulse-assisted probe immobilization followed by MCH backfill for probe concentration of 0.0625 µM, 0.125 µM and 0.5 µM, respectively; (D) insertion method; (E) co-deposition method.

These results suggest that uniform films with well-separated dsDNA (as is the case for insertion and co-deposition) melt slightly faster when bound to cisplatin, but to a lesser extent.

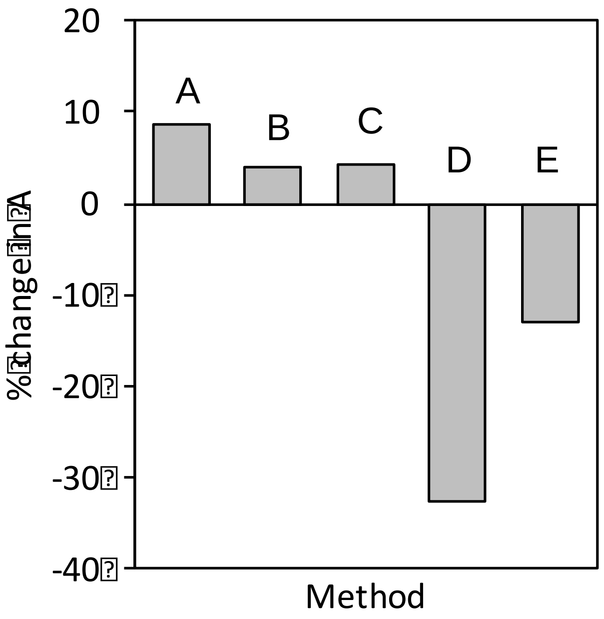

**Figure 47:** Comparison of the % change in A upon binding of cis-Pt for various electrode modification methods: (A), (B), (C) Pulse-assisted probe immobilization followed by MCH backfill for probe concentration of 0.0625 µM, 0.125 µM and 0.5 µM, respectively; (D) insertion method; (E) co-deposition method.

The % change in *tau* for all five preparation methods is shown in Figure 46. The binding of DNA by cisplatin is expected to decrease thermal stability, particularly at higher ionic strength [45]. In films prepared via insertion (D) and co-deposition (E), ionic strength within the layer is expected to be higher than in solution, particularly under the application of a negative potential. The slight decrease in *tau* suggests that in these films, cisplatin primarily cross-links bases on the same duplex, destabilizing the DNA and allowing it to melt faster. Previously, we have shown that mismatches in the DNA also lead to smaller *tau* values due to destabilization [32]. The drastic decrease in the extent of melting as shown in Figure 47 (D and E) may be explained by significant interstrand binding of cisplatin at some duplexes, effectively “tethering” the two strands together, preventing release of targets into solution.

The increased *tau* for films prepared via backfilling (see Figure 47, A-C) is caused by cross-linking between neighboring duplexes, inducing an increase in rigidity as has recently been observed using QCM measurements [48]. In that report the authors used the backfill method to generate mixed monolayers of DNA and MCH with coverages of $3.13 \times 10^{12}$ to $3.523 \times 10^{12}$. In our work here, the surface coverages of the films adsorbed via backfilling have surface densities of $4.4 \times 10^{12}$ to $7.3 \times 10^{12}$ targets/cm$^2$ as determined from cyclic voltammetry. If these films were uniform, these coverages would correspond to interstrand distances of approximately 5.4 to 4.2 nm, respectively. The contour length of the 18-bp duplex is about 5.4 nm (given a 0.3 nm rise per base pair) and the 6-carbon linker is ca. 0.8 nm. DNA duplexes with MCH passivation layers are known to stand approximately perpendicular to the surface (depending on the surface charge) [88-90]. Furthermore, short DNA duplexes like those used here are rigid [91]. Given this, it is unlikely that uniform films at these densities could be readily cross-linked by cisplatin. But, backfilling with MCH is expected to result in heterogeneous surface coverages, resulting in regions of densely packed DNA, or aggregates, where cisplatin can more easily cross-link the strands, increase rigidity, and ultimately make the DNA monolayer slower to melt in electric fields as evidenced by the large increases in tau. The slight increase in the extent of melting indicates that these films are no more stable in the high electric fields. To the contrary, they are slightly destabilized, resulting in a higher melting efficiency, although at a slower rate.

### *Conclusion*

Here we have studied the effect of anti-tumor drug cisplatin on the electrochemical melting of DNA. By applying a purely electrochemical routine, the electric-field-induced melting of dsDNA with and without cisplatin was monitored as a function of time. The voltammetric peak currents were plotted versus time to construct melting curves which were fit by an exponential function with two parameters, the time constant, *tau*, and the extent of melting, *A*. Three commonly used methods to prepare DNA monolayers were compared: the backfill method, consisting of pulse-assisted adsorption of probe DNA followed by MCH; the insertion method, consisting of adsorption of MCH followed by DNA; and the co-deposition method, consisting of the pulse-assisted adsorption of both MCH and DNA simultaneously.

Overall, the effect of cisplatin was found to depend significantly on the method used to prepare the monolayer. For co-deposition and insertion, which are assumed to produce more homogenous surface coverages, the extent of melting and the time constant were decreased by the presence of cisplatin, with the extent being most effected. On the other hand, for the backfill method cisplatin resulted in an increase in both time constant and extent of melting, with the effect being most pronounced for the time constant. These results suggest that the mode of DNA cross-linking by cisplatin is highly dependent on the DNA surface coverage, heterogeneity, and interstrand distances. Additionally, these results give a first glimpse into the role of surface density and heterogeneity effecting electrochemical melting in general – factors not yet fully explored, and which are expected to provide insights into DNA stability in high electric fields. In overview, these insights should be useful for interpretation of other electrochemical DNA biosensing results which rely on hybridization, melting, and binding of DNA to small molecules at electrode surfaces.

# Conclusion

In this thesis, we have improved on the electrostatic denaturation routine introduced in previous research [32]. The combination of the RuHex assay and potential assisted pulsing allows for the quantification of molecules per $cm^2$ using the MB signal. Also, surface coverage can be controlled precisely by altering the probe concentration and pulse time. Depending on the surface coverage, the extent and rate of electrostatic denaturation changes. Different ionic strengths change the rate and extent of melting, and the MB signal obtained. The largest stabilization can be seen at 500 mM NaCl. The introduction of the pulse melting routine allows for a faster melt than previously used methods. The optimization techniques obtained allows for accurate observation of cisplatin-DNA interactions on a gold biosensor. By changing the preparation of the DNA monolayer, a more homogenous surface leads to a decreased extent of melting, while a less homogenous surface leads to an increase in the extent of melting. These results suggest that cross-linking is highly dependent on surface coverage. Cross-linked DNA makes the DNA more rigid and, therefore, harder to melt. So, a decrease in the extent of melting is most likely caused by interstrand cross-linking. To better understand this observation, more studies will need to be performed exploring the effect of surface homogeneity on electrostatic denaturation. Other factors can also be introduced, such as temperature and different pulse melting parameters, to optimize electrostatic denaturation further. Once optimized, other platinum-based drugs could potentially be detected using our techniques.

## References

1. Cosnier, S. *Electrochemical biosensors;* Pan Stanford series on the high-tech of biotechnology; Pan Stanford Pub: Stanford, 2015; Vol. 3.
2. Wang, J. Electrochemical Glucose Biosensors. *Chemical Reviews* **2008**, *108*, 814-825.
3. Rowe, C. A.; Scruggs, S. B.; Feldstein, M. J.; Golden, J. P.; Ligler, F. S. An Array Immunosensor for Simultaneous Detection of Clinical Analytes. *Analytical Chemistry* **1999**, *71*, 433-439.
4. V, K. DNA Biosensors-A Review. *Journal of Bioengineering & Biomedical Science* **2017**, *7*.
5. LibreTexts Electrochemistry Basics (accessed July 15, 2019).
6. LibreTexts Electrolytic Cell (accessed July 15, 2019).
7. Elgrishi, N.; Rountree, K. J.; McCarthy, B. D.; Rountree, E. S.; Eisenhart, T. T.; Dempsey, J. L. A Practical Beginner's Guide to Cyclic Voltammetry. *Journal of Chemical Education* **2018**, *95*, 197-206.
8. LibreTexts Nernst Equation (accessed September 20, 2019)
9. Bard J. Allen; Faulkner R. Larry *Electrochemical Methods * 2001
10. Bijoy Bhattacharyya *Chapter 2 - Electrochemical Machining: Macro to Micro;* 2015; pp 25-32.
11. Square Wave Voltammetry  Gamry Instruments; *https://www.gamry.com/application-notes/physechem/square-wave-voltammetry/* (accessed July 18th, 2019).
12. Chronoamperometry/chronocoulometry. *https://www.basinc.com/manuals/EC_epsilon/Techniques/ChronoI/ca* (accessed July 18th, 2019).
13. History of DNA  *https://www.lunadna.com/blog/history-of-dna/*.
14. WATSON, J., CRICK, F. Molecular Structure of Nucleic Acids: A Structure for Deoxyribose Nucleic Acid. Nature 171, 737–738 (1953) doi:10.1038/171737a0
15. Alberts B, Johnson A, Lewis J, et al. Molecular Biology of the Cell. 4th edition. New York: Garland Science; 2002. The Structure and Function of DNA.
16. Clark Jim, DNA Structure. *https://www.chemguide.co.uk/organicprops/aminoacids/dna1.html* (accessed 10/30/2019)
17. Hardison Ross; Libre Texts B-Form, A-Form, and Z-Form of DNA.
18. Anonymous Cells Can Replicate Their DNA Precisely; *Nature Education* **2014**.
19. Anonymous What is DNA replication? (accessed 10/31/, 2019)
20. Anonymous What kinds of gene mutations are possible? *https://ghr.nlm.nih.gov/primer/mutationsanddisorders/possiblemutations*.
21. *1120 Wiley-VCH Verlag GmbH & Co. KGaA, Weinheim*.Web.
22. "Application Handbook." *Application handbook*Web.
23. "Current Protocols Essential Laboratory Techniques." *Journal of Technology*: 325. Jul 21, 2008. Web.
24. Ferreira, Isabel D., Virgílio E. do Rosário, and Pedro V. L. Cravo. "Real-Time Quantitative PCR with SYBR Green I Detection for Estimating Copy Numbers of Nine Drug Resistance Candidate Genes in Plasmodium Falciparum." *Malaria journal* 5.1 (2006): 1. *MEDLINE.* Web.
25. Ramakers, Christian, et al. "Assumption-Free Analysis of Quantitative Real-Time Polymerase Chain Reaction (PCR) Data." *Neuroscience Letters* 339.1 (2003): 62-6. *MEDLINE.* Web.
26. Safeukui, I.; Millet, P.; Boucher, S.; Melinard, L.; Fregeville, F.; Receveur, M.; Pistone, T.; Fialon, P.; Vincendeau, P.; Fleury, H.; Malvy, D. Evaluation of FRET real-time PCR assay for rapid detection and differentiation of Plasmodium species in returning travellers and migrants. *Malaria journal* **2008**, *7*, 70.

27. Schmittgen, Thomas D. "Real-Time Quantitative PCR." *Methods* 25.4 (2001): 383-5. *MEDLINE.* Web.
28. *Simultaneous Amplification and Detection of Specific DNA Sequences*., 1992. Web.
29. Ren, Y.; Deng, H.; Shen, W.; Gao, Z. A Highly Sensitive and Selective Electrochemical Biosensor for Direct Detection of MicroRNAs in Serum. **2013**.
30. Stephen S W Yeung; Thomas M H Lee; I-Ming Hsing Electrochemistry-Based Real-Time PCR on a Microchip. *Analytical Chemistry* **2008**, *80*, 363-368.
31. Papadopoulou, E.; Goodchild, S. A.; Cleary, D. W.; Weller, S. A.; Gale, N.; Stubberfield, M. R.; Brown, T.; Bartlett, P. N. Using Surface-Enhanced Raman Spectroscopy and Electrochemically Driven Melting to Discriminate Yersinia pestis from Y. pseudotuberculosis Based on Single Nucleotide Polymorphisms within Unpurified Polymerase Chain Reaction Amplicons. *Analytical Chemistry* **2015**
32. Ho, D.; Hetrick, W.; Le, N.; Chin, A.; West, R. M. Editors' Choice—Electric Field-Induced DNA Melting with Detection by Square Wave Voltammetry. *Journal of The Electrochemical Society* **2019**, *166*, B236-B242.
33. Steel, A. B.; Herne, T. M.; Tarlov, M. J. Electrochemical Quantitation of DNA Immobilized on Gold. *Analytical Chemistry* **1998**, *70*, 4670-4677.
34. Jambrec, D.; Gebala, M.; La Mantia, F.; Schuhmann, W. Potential-Assisted DNA Immobilization as a Prerequisite for Fast and Controlled Formation of DNA Monolayers. *Angewandte Chemie International Edition* **2015**, *54*, 15064-15068.
35. Jambrec, D.; Conzuelo, F.; Estrada-Vargas, A.; Schuhmann, W. Potential-Pulse-Assisted Formation of Thiol Monolayers within Minutes for Fast and Controlled Electrode Surface Modification. *ChemElectroChem* **2016**, *3*, 1484-1489.
36. Nevena Tomic Chemical Science. **2019**.
37. . Anonymous The "Accidental" Cure—Platinum-based Treatment for Cancer: The Discovery of Cisplatin. (accessed November 27, 2019).
38. Alderden, R. A.; Hall, M. D.; Hambley, T. W. The Discovery and Development of Cisplatin. Journal of Chemical Education 2006, 83, 728.
39. Y. Zhang, Z. Guo, X.Z. You, Hydrolysis theory for cisplatin and its analogues based on density functional studies, Journal of the American Chemical Society 123 (2001) 9378-9387. https://doi.org/10.1021/ja0023938
40. Y. Mantri, S.J. Lippard, M.H. Baik, Bifunctional binding of cisplatin to DNA: why does cisplatin form 1, 2-intrastrand cross-links with AG but not with GA?, Journal of the American Chemical Society 129 (2007) 5023-5030. https://doi.org/10.1021/ja067631z
41. M.H. Baik, R.A. Friesner, S.J. Lippard, Theoretical study of cisplatin binding to purine bases: why does cisplatin prefer guanine over adenine?, Journal of the American Chemical Society 125 (2003), 14082-14092. https://doi.org/10.1021/ja036960d
42. S.E. Sherman, S.J. Lippard, Structural aspects of platinum anticancer drug interactions with DNA, Chemical Reviews 87 (1987) 1153-1181. https://doi.org/10.1021/cr00081a013
43. N. Poklar, D.S. Pilch, S.J. Lippard, E.A. Redding, S.U. Dunham, K.J. Breslauer, Influence of cisplatin intrastrand crosslinking on the conformation, thermal stability, and energetics of a 20-mer DNA duplex, Proceedings of the National Academy of Sciences 93 (1996) 7606-7611. https://doi.org/10.1073/pnas.93.15.7606
44. C.L. Chang, D.Y. Lando, A.S. Fridman, C.K. Hu, Thermal stability of DNA with interstrand crosslinks, Biopolymers 97 (2012) 807-817. https://doi.org/10.1002/bip.22077
45. R. Žaludová, V. Kleinwächter, V. Brabec, The effect of ionic strength on melting of DNA modified by platinum (II) complexes, Biophysical chemistry 60 (1996), 135-142. https://doi.org/10.1016/0301-4622(96)00010-5

46. Graziana Bagni; Mauro Ravera; Domenico Osella; Marco Mascini Electrochemical Biosensors as a Screening Tool of In Vitro DNA-Drug Interaction. Current Pharmaceutical Analysis 2005, 1, 217-224.
47. P. Horáková, L. Těsnohlídková, L. Havran, P. Vidláková, H. Pivoňková, M. Fojta, Determination of the level of DNA modification with cisplatin by catalytic hydrogen evolution at mercury-based electrodes, Analytical chemistry, 82 (2010), 2969-2976. https://doi.org/10.1021/ac902987x
48. S.K.K Galagedera, G.U. Flechsig, Detection of the Level of DNA cross-linking with Cisplatin by Electrochemical Quartz Crystal Microbalance, J. Electroanal. Chem. (2019) submitted.
49. U. Rant, K. Arinaga, S. Fujita, N. Yokoyama, G. Abstreiter, M. Tornow, Electrical manipulation of oligonucleotides grafted to charged surfaces, Organic & biomolecular chemistry 4 (2006) 3448-3455. https://doi.org/10.1039/B605712H
50. S. Mahajan, J. Richardson, T. Brown, P.N. Bartlett, SERS-Melting: A New Method for Discriminating Mutations in DNA Sequences, Journal of the American Chemical Society 130 (2008) 15589−15601. https://doi.org/10.1021/ja805517q
51. F. Wei, C. Chen, L. Zhai, N. Zhang, X.S. Zhao, Recognition of single nucleotide polymorphisms using scanning potential hairpin denaturation, Journal of the American Chemical Society 127 (2005), 5306-5307. https://doi.org/10.1021/ja043661v
52. R.J. Heaton, A.W. Peterson, R.M. Georgiadis, Electrostatic Surface Plasmon Resonance: Direct Electric Field-Induced Hybridization and Denaturation in Monolayer Nucleic Acid Films and Label-Free Discrimination of Base Mismatches, Proc. Natl. Acad. Sci. U. S. A. 98 (2001) 3701−3704. https://doi.org/10.1073/pnas.071623998
53. P. Li, Y. Chen, L. Wang, W. Lu, W. Li, K. Chen, Y. Zhou, L. Shen, F. Wei, W. Zheng, The electric double layer structure modulates poly-dT 25 conformation and adsorption kinetics at the cationic lipid bilayer interface, Soft matter, 15 (2019) 4445-4453. https://doi.org/10.1039/c9sm00321e
54. T. Siebert, B. Guchhait, Y. Liu, B.P. Fingerhut, T. Elsaesser, Range, magnitude, and ultrafast dynamics of electric fields at the hydrated DNA surface, The journal of physical chemistry letters, 7 (2016), 3131-3136. https://doi.org/10.1021/acs.jpclett.6b01369
55. R.P. Johnson, J.A. Richardson, T. Brown, P.N. Bartlett, Real-Time Surface-Enhanced Raman Spectroscopy Monitoring of Surface pH during Electrochemical Melting of Double-Stranded DNA, Langmuir, 28 (2012) 5464-5470. https://doi.org/10.1021/la204794g
56. R.P. Johnson, N. Gale, J.A. Richardson, T. Brown, P.N. Bartlett, Denaturation of dsDNA immobilised at a negatively charged gold electrode is not caused by electrostatic repulsion, Chemical Science, 4 (2013) 1625-1632. https://doi.org/10.1039/c3sc22147d
57. R. Levicky, A. Horgan, Physicochemical perspectives on DNA microarray and biosensor technologies, Trends in biotechnology, 23 (2005) 143-149. https://doi.org/10.1016/j.tibtech.2005.01.004
58. A.W. Peterson, R.J. Heaton, R. M. Georgiadis, The effect of surface probe density on DNA hybridization, Nucleic acids research 29 (2001) 5163-5168. https://doi.org/10.1093/nar/29.24.5163
59. A. Vainrub, and B.M. Pettitt, Accurate prediction of binding thermodynamics for DNA on surfaces, The Journal of Physical Chemistry B 115 (2011) 13300-13303. https://doi.org/10.1021/jp208141g
60. U. Rant, K. Arinaga, S. Fujita, N. Yokoyama, G. Abstreiter, M. Tornow, Dynamic electrical switching of DNA layers on a metal surface, Nano Letters, 4 (2004) 2441-2445. https://doi.org/10.1021/nl0484494

61. I.Y. Wong, and N.A. Melosh, An electrostatic model for DNA surface hybridization, Biophysical journal, 98 (2010), 2954-2963. https://doi.org/10.1016/j.bpj.2010.03.017
62. S.G. Ray, H. Cohen, R. Naaman, Y. Rabin, Where is the sodium in self-assembled monolayers of single-stranded DNA?, Journal of the American Chemical Society 127 (2005) 17138-17139. https://doi.org/10.1021/ja055201n
63. D. Bizzotto, I.J. Burgess, T. Doneux, T. Sagara, H.Z. Yu, Beyond simple cartoons: challenges in characterizing electrochemical biosensor interfaces, ACS sensors 3 (2018) 5-12. https://doi.org/10.1021/acssensors.7b00840
64. E.A. Josephs, T. Ye, Electric-field dependent conformations of single DNA molecules on a model biosensor surface, Nano letters, 12 (2012) 5255-5261. https://doi.org/10.1021/nl3024356
65. A. Halperin, A. Buhot, E.B. Zhulina, On the hybridization isotherms of DNA microarrays: The Langmuir model and its extensions, Journal of Physics: Condensed Matter, 18 (2006) S463-S490. doi:10.1088/0953-8984/18/18/s01
66. F. Wei, P. Qu, L. Zhai, C. Chen, H. Wang, X.S. Zhao, Electric Potential Induced Dissociation of Hybridized DNA with Hairpin Motif Immobilized on Silicon Surface, Langmuir, 22 (2006) 6280-6285. https://doi.org/10.1021/la060602h
67. J.H. Watterson, P.A.E. Piunno, C.C. Wust, U.J. Krull, Effects of oligonucleotide immobilization density on selectivity of quantitative transduction of hybridization of immobilized DNA, Langmuir, 16 (2000) 4984-4992. https://doi.org/10.1021/la991508m
68. J.H. Watterson, P.A.E. Piunno, U.J. Krull, Towards the optimization of an optical DNA sensor: control of selectivity coefficients and relative surface affinities, Analytica Chimica Acta 457 (2002) 29-38. https://doi.org/10.1016/S0003-2670(01)01304-6
69. J.N. Murphy, A.K.H. Cheng, H.Z. Yu, D. Bizzotto, On the Nature of DNA Self-Assembled Monolayers on Au: Measuring Surface Heterogeneity with Electrochemical in Situ Fluorescence Microscopy, J. Am. Chem. Soc., 131 (2009) 4042−4050. https://doi.org/10.1021/ja808696p
70. E.A. Josephs, T. Ye, Nanoscale spatial distribution of thiolated DNA on model nucleic acid sensor surfaces, Acs Nano, 7 (2013) 3653-3660. https://doi.org/10.1021/nn400659m
71. S. Ruffin, I.A. Hung, U.M. Koniges, R. Levicky, Electrostatic Cycling of Hybridization Using Nonionic DNA Mimics, ACS Sens., 2 (2017) 892−896. https://doi.org/10.1021/acssensors.7b00100
72. T.M. Herne, M.J. Tarlov, Characterization of DNA probes immobilized on gold surfaces, Journal of the American Chemical Society, 119 (1997) 8916-8920. https://doi.org/10.1021/ja9719586
73. K. Arinaga, U. Rant, M. Tornow, S. Fujita, G. Abstreiter, N. Yokoyama, The role of surface charging during the coadsorption of mercaptohexanol to DNA layers on gold: direct observation of desorption and layer reorientation, Langmuir, 22 (2006) 5560-5562. https://doi.org/10.1021/la060324m
74. U. Rant, K. Arinaga, S. Fujita, N. Yokoyama, G. Abstreiter, M. Tornow, Structural properties of oligonucleotide monolayers on gold surfaces probed by fluorescence investigations, Langmuir, 20 (2004) 10086-10092. https://doi.org/10.1021/la0492963
75. R. Lao, S. Song, H. Wu, L. Wang, Z. Zhang, L. He, C. Fan, Electrochemical interrogation of DNA monolayers on gold surfaces, Analytical chemistry, 77 (2005) 6475-6480. https://doi.org/10.1021/ac050911x
76. J.N. Murphy, A.K.H. Cheng, H.Z. Yu, D. Bizzotto, On the nature of DNA self-assembled monolayers on Au: measuring surface heterogeneity with electrochemical in situ fluorescence microscopy, Journal of the American Chemical Society, 131 (2009) 4042-4050. https://doi.org/10.1021/ja808696p
77. A. Meunier, E. Triffaux, D. Bizzotto, C. Buess-Herman, T. Doneux, In-Situ Fluorescence Microscopy Study of the Interfacial Inhomogeneity of DNA Mixed Self-Assembled Monolayers at Gold Electrodes, ChemElectroChem, 2 (2015) 434−442. https://doi.org/10.1002/celc.201402273

78. K. Arinaga, U. Rant, M. Tornow, S. Fujita, G. Abstreiter, N. Yokoyama, The role of surface charging during the co-adsorption of mercaptohexanol to DNA layers on gold: direct observation of desorption and layer reorientation, Langmuir, 22 (2006) 5560-5562. https://doi.org/10.1021/la060324m
79. T. Doneux, A. De Rache, E. Triffaux, A. Meunier, M. Steichen, C. Buess-Herman, Optimization of the Probe Coverage in DNA Biosensors by a One-Step Coadsorption Procedure, ChemElectroChem, 1 (2014) 147-157. https://doi.org/10.1002/celc.201300145
80. Z.L. Yu, C.W.T. Yang, E. Triffaux, T. Doneux, R.F.B. Turner, D. Bizzotto, Measuring and Remediating Nonspecific Modifications of Gold Surfaces Using a Coupled in Situ Electrochemical Fluorescence Microscopic Methodology, Anal. Chem., 89 (2017) 886−894. https://doi.org/10.1021/acs.analchem.6b03953
81. A.M. Spehar-Deleze, L. Schmidt, R. Neier, S. Kulmala, N. de Rooij, M. Koudelka-Hep, Electrochemiluminescent hybridization chip with electric field aided mismatch discrimination, Biosensors and Bioelectronics, 22 (2006) 722-729. https://doi.org/10.1016/j.bios.2006.02.013
82. I.Y. Wong, N.A. Melosh, Directed Hybridization and Melting of DNA Linkers using Counterion-Screened Electric Fields, NanoLetters, 9 (2009) 3521-3526. https://doi.org/10.1021/nl901710n
83. R. Georgiadis, K.P. Peterlinz, A.W. Peterson, Quantitative measurements and modeling of kinetics in nucleic acid monolayer films using SPR spectroscopy, Journal of the American Chemical Society, 122 (2000) 3166-3173. https://doi.org/10.1021/ja9930824
84. P. Gong, R. Levicky, DNA Surface Hybridization Regimes, Proc. Natl. Acad. Sci. U. S. A., 105 (2008) 5301-5306. https://doi.org/10.1073/pnas.0709416105
85. N. Tercero K. Wang, P. Gong, R. Levicky, Morpholino monolayers: preparation and label-free DNA analysis by surface hybridization, Journal of the American Chemical Society, 131 (2009) 4953-4961. https://doi.org/10.1021/ja810051q
86. M. Meneghello, E. Papadopoulou, P. Ugo, P.N. Bartlett, Using electrochemical SERS to measure the redox potential of drug molecules bound to dsDNA—a study of mitoxantrone, Electrochimica Acta, 187 (2016), 684-692. https://doi.org/10.1016/j.electacta.2015.11.121
87. S.M. Robinson, Z. Shen, J.R. Askim, C.B. Montgomery, H.O. Sintim, S. Semancik, Ligand-Based Stability Changes in Duplex DNA Measured with a Microscale Electrochemical Platform. Biosensors, 9, (2019) 54. https://doi.org/10.3390/bios9020054
88. S.O. Kelley, J.K. Barton, N.M. Jackson, L.D. McPherson, A.B. Potter, E.M. Spain, M.J. Allen, M.G. Hill, Orienting DNA helices on gold using applied electric fields, Langmuir, 14 (1998) 6781-6784. https://doi.org/10.1021/la980874n
89. Z.L. Zhang, D.W. Pang, R.Y. Zhang, J.W. Yan, B.W. Mao, Y.P. Qi, Investigation of DNA orientation on gold by EC-STM, Bioconjugate chemistry, 13 (2002) 104-109. https://doi.org/10.1021/bc0155263
90. L.Q. Dong, J.Z. Zhou, L.L. Wu, P. Dong, Z.H. Lin, SERS studies of self-assembled DNA monolayer–characterization of adsorption orientation of oligonucleotide probes and their hybridized helices on gold substrate, Chemical physics letters, 354 (2002) 458-465. https://doi.org/10.1016/S0009-2614(02)00163-X
91. J. Bednar, P. Furrer, V. Katritch, A.Z. Stasiak, J. Dubochet, A. Stasiak, Determination of DNA Persistence Length by Cryo-electron Microscopy. Separation of the Static and Dynamic Contributions to the Apparent Persistence Length of DNA, J. Mol. Biol., 254 (1995) 579-594. https://doi.org/10.1006/jmbi.1995.0640